Atlantic Warm Pool Variability in the CMIP5 Simulations

Hailong Liu[1,2], Chunzai Wang[2], Sang-Ki Lee[1,2], David Enfield[1,2]

[1] Cooperative Institute for Marine and Atmospheric Studies, University of Miami, Miami FL

[2] Atlantic Oceanographic and Meteorological Laboratory, NOAA, Miami FL

Accepted by Journal of Climate

2012

Corresponding author: Hailong Liu,
RSMAS/CIMAS,
4600 Rickenbacker Causeway
Miami, FL 33149
Email: Hailong.liu@noaa.gov

Abstract

This study investigates Atlantic Warm Pool (AWP) variability in the historical run of 19 coupled general circulation models (CGCMs) submitted to phase five of the Coupled Model Intercomparison Project (CMIP5). As with the CGCMs in CMIP3, most models suffer from the cold SST bias in the AWP region, and also show very weak AWP variability represented by AWP area index. However, for the seasonal cycle the AWP SST bias of model ensemble and model sensitivities are decreased compared with CMIP3, indicating that the CGCMs are improved. The origin of the cold SST bias in the AWP region remains unknown, but among the CGCMs in CMIP5 excess (insufficient) high-level clouds simulation deceases (enhances) the cold SST bias in the AWP region through the warming effect of the high-level clouds radiative forcing. Thus the AWP SST bias in CMIP5 is more modulated by an erroneous radiation balance due to misrepresentation of high-level clouds rather than low-level clouds as in CMIP3. AWP variability is assessed as in our previous study in the aspects of spectral analysis, interannual variability, multidecadal variability and comparison of the remote connections with ENSO and the NAO against observations. In observations the maximum influences of the NAO and ENSO on the AWP take place in boreal spring. For some CGCMs these influences erroneously last to late summer. The effect of this overestimated remote forcing can be seen in the variability statistics as shown in the rotated EOF patterns from the models. We conclude that NCAR-CCSM4, GISS-E2H and GISS-E2R are the best three models of CMIP5 in simulating AWP variability.

1. Introduction

The Atlantic Warm Pool (AWP), defined as the region with sea surface temperature (SST) above 28.5^{o}C consisting of the Gulf of Mexico, the Caribbean Sea and the western tropical North Atlantic, undergoes strong variations on seasonal to multidecadal time scales (Wang and Enfield 2001, 2003; Wang et al. 2008, Enfield and Cid-Serrano 2010). The AWP variability has been shown to play a role in the climate system by affecting precipitation patterns and tropical cyclone activity (Wang et al. 2006; Wang et al. 2008a; Wang et al. 2008b; Wang et al. 2011), so it is important to evaluate how well coupled general circulation models (CGCMs) represent this variability. Liu et al. (2012) (hereafter referred to as LWLE12) have studied the AWP variability against observations in 22 CGCMs from phase three of the Coupled Model Intercomparison Project (CMIP3), concluding that most CMIP3 CGCMs suffer from a marked cold SST bias in the AWP region but that there is always one group of CGCMs that are able to represent well each aspect of AWP variability, although each aspect is reproduced by a different set of models. This paper extends the AWP variability study in the new generation of CGCMs provided by phase five of the Coupled Model Intercomparison Project (CMIP5) and assesses the model progress as compared with CMIP3.

The AWP develops in June, reaches its maximum during the four months of July, August, September and October, and decays quickly after October (Wang and Enfield 2003). For this annual cycle, Enfield and Lee (2005) showed that the AWP variation is largely forced by the shortwave radiation, while the latent heat flux plays a secondary role particularly during the AWP decay phase. This seasonal cycle in many of the CMIP3 models has significant cold bias in the AWP region (Chang et al. 2007, Chang et al. 2008, Richter and Xie 2008, Misra et al. 2009, Richter et al. 2012, LWLE12). Large and Danabasoglu (2006) and Chang et al. (2007) both

pointed that the North Atlantic subtropical high and associated surface winds are stronger than observed. Grodsky et al. (2012) further examined the tropical Atlantic SST bias based on the Community Climate System Model version 4 (CCSM4) and pointed out that the excess winds induced by erroneously high sea level pressure (SLP) cause excess surface latent heat loss and cold SST bias in the tropical North Atlantic (NTA). However, based on an analysis of observed air-sea fluxes Misra et al. (2008) found that surface evaporation in the AWP region is weakly influenced by both surface winds and air-sea humidity variations, while in the National Centers for Environmental Prediction (NCEP) Climate Forecast System (CFS) the latent heat flux is only strongly modulated by the air-sea humidity variations. These studies indicate that unlike in the NTA, increased winds and evaporation cannot fully explain the cold SST bias in the AWP region. Li and Xie (2012) summarized that the tropical SST bias can be classified into two types: one type with the same sign across all basins that is highly correlated with the tropical mean caused by biases in atmospheric simulations of cloud cover, the other type with large variability in the cold tongue regions caused by biases of oceanic thermocline depth. The AWP bias is more related to radiative flux errors due to local convection and clouds (LWLE12).

As the AWP is adjacent to the NTA and in fact includes the western NTA (NTA is defined as the region of 5.5^0N-23.5^0N and 57.5^0W-15^0W), climate variability of the AWP is contemporaneously correlated with variability in the NTA to the east (Wang and Enfield, 2003). Thus the major modes of the tropical Atlantic variability contribute to the AWP interannual and longer time scales. The correlations of the AWP with the tropical Atlantic meridional gradient mode (AMM) (Servain 1991; Chang et al. 1997, Xie et al. 1999; Enfield et al. 1999; Xie and Carton 2004) and the Atlantic Niño (Zebiak 1993; Carton and Huang 1994; Latif and Grotzner 2000; Okumura and Xie 2006) are statistically significant but relatively low compared with the

correlations of the AWP with Niño-3 (5°S–5°N, 150°–90°W) SST anomalies and NTA SST anomalies, suggesting that the impacts of the AMM and the Atlantic Niño on the AWP are weaker than those of the Pacific El Niño and NTA (Wang and Enfield 2003). The different correlation of the AWP with AMM and NTA is consistent with the observation of Enfield et al (1999) that the NTA and tropical South Atlantic are uncorrelated at zero lag and show different timescales of variability. Through rotated Empirical Orthogonal Functions (rEOFs) statistical analysis, the southern tropical Atlantic (STA) pattern, northern tropical Atlantic (NTA) pattern, and subtropical South Atlantic (SSA) pattern are three major modes exhibited (Huang and Shukla 2005; Bates 2008). In CGCMs, however, the STA mode may demonstrate two separate patterns in the tropical South Atlantic. The mode with variability in the southern segment of the Benguela upwelling zone off the coast of Namibia is subcategorized as STA-BG mode and the mode of equatorial tongue pattern is subcategorized as STA-EQ mode (Muñoz et al., 2012). The separation of STA-BG and STA-EQ in numerical models unlike the observations is related to the model systematic bias of excessive southward shift of the intertropical convergence zone to around 10°S in boreal spring (Huang et al. 2004). Excessive southward shift of the Atlantic ITCZ in CMIP3 model and its relation to the weak bias of the southerly wind along the African coast are also discussed by Richter and Xie (2008); Hu et al. (2008) and Doi et al. (2010). Tozuka et al. (2011) showed that the tropical Atlantic bias is highly sensitive to the choices of deep convection parameterization.

Another issue related to model performance and assessment is the extent to which the models reproduce the observed manner in which climate modes appear to force changes in the AWP. Much more of the NTA variability is caused by remote forcing from climate variability outside the tropical Atlantic than by the intrinsic self-sustained modes of the tropical Atlantic

variablity (Xie and Carton, 2004). Czaja et al. (2002) showed that almost all NTA-SST extreme events can be related to either ENSO or the NAO, consistent with Enfield et al. (2006). Analysis based on NOAA-CIRES Twentieth Century Global Reanalysis (20CR) indicates that both positive ENSO phase and the negative NAO phase in winter correspond to reduced trade winds in the AWP region (LWLE12). The westerly anomalies induced by positive ENSO and the negative NAO, associated also with increased sea level pressure and subsidence in the NTA, lead to local heating through reduced latent heat loss, ultimately leading to warm SST during March to May (ENSO) and February to April (NAO). This behavior is a known feature of anomalous AWP growth and well captured by only 5 models out of 22 CGCMs in CMIP3 (LWLE12).

The Atlantic Multidecadal Oscillation (AMO) (Delworth and Mann 2000; Enfield et al. 2001; Bell and Chelliah 2006) is an oscillatory mode occurring in the North Atlantic SST primarily on multidecadal timescales. Wang et al. (2008) showed that the AWP variability coincides with the signal of the AMO “the warm (cool) phases of the AMO correspond to more large (small) AWPs” and suggested that the multidecadal influence of the AMO on Atlantic tropical cyclone activity (Goldenberg et al. 2001) may operate through the mechanism of the AWP-induced atmospheric changes. In CMIP3, the global SST difference pattern between large AWP years and small AWP years on the multidecadal timescale resembles the geographic pattern of the AMO for most coupled models (LWLE12).

Many studies have been conducted to evaluate the performance of CGCMs in World Climate Research Program (WCRP) CMIP3 multi-model dataset (e.g., Saji et al. 2006; Joseph and Nigam 2006; Chang et al. 2007; Ritchter and Xie 2008; de Szoeke and Xie 2008; Wang et al. 2009). As the CMIP5 model dataset is now available, it is of interest to evaluate how well the new generation of CGCMs represents AWP variability in order to improve and apply coupled

climate models for AWP research. In this study we analyzed 19 state-of-the-art CGCMs in the WCRP CMIP5 multimodel dataset as to how they replicate AWP variability from seasonal to multidecadal time scales as well as the AWP's teleconnection with ENSO and the NAO. The remainder of the paper is organized as follows. The models, validation datasets and methods used in this study are described in section 2. The AWP seasonal cycle and bias analysis are included in section 3. The AWP variability of interannual and longer timescales in CGCMs is studied and compared with observations and CMIP3 simulations in section 4. Section 5 summarizes the conclusions.

2. Data and methods

This study is based on output from historical simulations of 19 CGCMs in WCRP CIMP5 multi-model dataset. The modeling center and country, CMIP5 model abbreviation and designated letter, and length of historical simulations for each model in this study are shown in Table 1. CMIP3 model abbreviations are also included for references in the table grouped by modeling center. The model data can be downloaded from the website of Program for Climate Model Diagnosis and Intercomparison (PCMDI) (http://www-pcmdi.llnl.gov/). The historical simulations are spun up and then forced by solar, volcanic, sulfate aerosol and greenhouse gas forcings (Meehl et al. 2007) from different starting years (1850, 1859, 1860, 1861) to 2005.

Observational datasets are used to validate the variabilities of CGCM simulations. SST data are the NOAA Extended Reconstruction Sea Surface Temperature version 3 (ERSST v3) (Smith et al. 2008). The temporal coverage is from January 1854 to the present. These data can be obtained from http://www.ncdc.noaa.gov/oa/climate/research/sst/ersstv3.php. Surface fluxes and SLP data are from NOAA-CIRES Twentieth Century Global Reanalysis (20CR) Version II

(Compo et al. 2010). This atmospheric reanalysis spans the entire twentieth century (1871-2008), assimilating only surface observations of synoptic pressure, monthly SST and sea ice distribution. More information about this dataset is provided in http://www.esrl.noaa.gov/psd/data/20thC_Rean/. Latent heat flux and surface winds from IFREMER are provided from ftp://ftp.ifremer.fr/ifremer/cersat/products/gridded/flux-merged (Bentamy et al. 2008). This entire 16-year (1992-2007) surface turbulent fluxes dataset estimated from satellite observations are improved from the previous version in assessing the surface winds from ERS-1, ERS-2, and QuickSCAT scatterometers and using the new NOAA sea surface temperature estimates.

The AWP area index（AWPAI) is defined as the area inside the 28.5°C isotherm at the sea surface in the AWP region. Due to the cold SST bias in CGCMs the AWPAI cannot be defined for all the models and in certain years. So the AWP SST index (AWPTI) is defined in this study as the box averaged SST from coast to 40˚W and from 5˚N to 30˚N. The AMO index is defined as the detrended area weighted average of the SST anomalies over the North Atlantic from 0˚N to 70˚N (Enfield et al. 2001). The Niño 3 index is an average of the SST anomalies in the region 150˚W - 90˚W and 5˚N to 5˚S. The NAO index is chosen as the difference of normalized SLP between 39˚N, 9˚W (Lisbon, Portugal) and 65˚N, 22˚W (Stykkisholmur/Reykjavik, Iceland) (Hurrell 1995). All indexes are calculated for each model and observations. The clouds are classified by cloud top height. The high level clouds are 400 hPa or over, the middle level clouds 400 to 600 hPa, and the low level clouds 600 hPa or less as in a rough standard. The cloud factions of the model outputs are integrated over these three layers separately to represent the low level, middle level and high level cloud amount.

Wavelet software for spectrum analysis was provided by C.Torrence and G. Compo

(Torrence and Compo 1998) for spectrum analysis. The Taylor diagram (Taylor 2001) is applied to quantify how well models simulate an observed climate field. It relies on three non-dimensional statistics: (1) the ratio of the variances of the two fields (r, which is the standard deviation of the model divided by standard deviation of the observations); (2) the correlation between the two fields (R, which is computed after removing the overall means); and (3) the root mean square error between models and observation (E, which is normalized by the standard deviation of the observed field). This diagram provides a 2-D graph based on the three statistics summarizing how closely a pattern matches observations.

3. AWP Climatology

a. Seasonal Cycle

The AWPAI of 19 models (In this study models (CGCMs) indicate the models from CMIP5 or general meaning unless CMIP3 follows) ensemble is slightly increased during July, August and September (JAS) compared with the ensemble of AWPAI in CMIP3 (Figure 1.a). Though the seasonal cycle of AWPAI ensemble with peaks in JASO is well simulated, it is still much underestimated compared with ERSST due to the cold SST bias in the AWP region (Misra et al. 2008; LWLE12). The bias of APWAI reaches -4.2 10^6 km^2 in summer, but almost no bias exists in January as there is no AWP in winter based on definition. The spread of models AWPAI contracts in contrast with the spread of CMIP3. The AWPAI of 10 models are less than 20% of ERSST AWPAI in summer and for some certain years AWPAI of a part of CGCMs cannot be computed to study their interannual and multidecadal variability due to the cold SST bias. Therefore, the AWPTI is used for this study.

Figure 1.b shows the AWPTI of model ensemble mean successfully representing the

seasonal cycle of ERSST which peaks in JASO. However, there is cold bias throughout all the year with minimum cold bias of 0.89^{o}C in January and maximum cold bias over 1.2^{o}C in MJJ. The spread is consistent for all the months with a range of 1.9-2.2^{o}C. Compared with CMIP3, the ensemble mean of AWPTI increases about 0.3^{o}C all year round (Figure 1.d) and the spread of models also contracts about 1°C. To some extent the performance of CMIP5 in simulating AWP seasonal cycle is improved from the view of model ensemble. The improvement of models ensemble mean may be explained by the slight increase of net surface heat flux in CMIP5 (Figure 1.d). Compared with CMIP3, the ensemble mean of net surface heat flux increases within a range of 1.5 W/m^2 to 3.4 W/m^2 during JJASO. This increase accounts for about 0.1^{o}C temperature change if we roughly estimate the mixed layer depth at about 25m in the AWP region. For each component of surface heat fluxes, the ensemble mean of CMIP5 has more latent heat loss (heat loss means that ocean loses heat, heat gain means that ocean gains heat), more longwave radiation loss, less sensible heat loss and more net shortwave radiation gain (Figure 1.d) compared with CMIP3. However, the ensemble mean of both CMIP3 (Figure 1.f) and CMIP5 (Figure 1.e) possesses the same sign of bias for each component of surface heat fluxes except net shortwave radiation given the reference of 20CR. Wang and Enfield (2001) suggested that the SST seasonal variations in the AWP region are induced primarily by surface net heat flux with a phase lag of 3-4 months. The shortwave and latent heat fluxes are two largest terms. The shortwave flux has maximum value from April to August, and the latent and sensible heat losses have their minima around May owing to lower winds speeds associated with the seasonal south-north movement of the ITCZ. Minimum longwave radiation occurs from July to September because greater cloud cover results in an increase in the downward longwave radiation from cloud ceilings. This results in the maximum of net heat flux occurring in late spring and

maximum SST in fall. These relationships between heat fluxes and AWP SST are well reflected in 20CR (Figure 1.c), CMIP3 and CMIP5 ensemble mean.

We categorize CMIP5 models into different groups based on their development institutions. For group of the GISS, both GISS-E2H and E2R have better performance in simulating the AWP seasonal cycle compared with previous generation of GISS-AOM and ER. The AWPTI bias of GISS-E2R (Figure 2.a) is much smaller than the GISS-ER (Figure 2.b). Compared with GISS-ER, the latent heat flux bias decreases the most in GISS-E2R. However, this decreased positive latent heat flux bias is not able to explain the decreased negative AWPTI bias. For group of the NCAR, CCSM4 (Figure 2.c) is much improved from CCSM3 (Figure 2.d) for the seasonal AWPTI simulation. Compared with CCSM3 for each component bias of surface heat fluxes, the shortwave heat flux bias changes the most in CCSM4. This increased shortwave heat flux in CCSM4 may explain the decreased negative AWPTI bias. Both GISS-E2R and CCSM4 improves the simulation of AWPTI from the last generation corresponding CGCMs, but the heat flux component bias analysis cannot give a consistency conclusion why the simulations are improved.

For group of the GFDL, GFDL-CM3 (Figure 2.e), ESM2G and ESM2M (not shown) of CMIP5 have no better performance in simulating the AWP seasonal cycle compared with GFDL-CM2 (Figure 2.f) of CMIP3. CM3 has a notable difference in seasonal cycle of surface heat fluxes compared with the other GFDL models. In summer, CM3 has less sensible heat loss, less longwave radiation loss and shortwave radiation gain, with the net heat flux peaking one month earlier than the other GFDL models (Figure 2.e-f).

For group of the CSIRO, the CSIRO-MK3.6 (Figure 2.g) of CMIP5 has larger AWPTI negative bias but also has larger positive net heat flux compared with CSIRO-MK 3.5 of

CMIP3 (not shown). The larger net heat flux of CSIRO-MK3.6 is not able to explain the weaker amplitude of AWPTI compared with MK3.5, which may indicate that oceanic processes play a role.

For the other goups of CGCMs, detail discussions are not included. In general no unanimous conclusions of how the surface fluxes components affect the AWPTI bias. But for some models such as GFDL-CM3 (2.e) GFDL-CM2 (2.f) and CSIRO-MK3.6 (2.g) the seasonal cycle of longwave radiation bias is highly correlated with AWPTI bias; for some models such as GISS-ER (2.b), CCSM3 (2.d) the seasonal cycle of shortwave radiation bias is correlated with AWPTI bias. Thus AWP SST bias in CGCMs possibly relate with different physical mechanisms associated with shortwave and longwave radiation.

In summary the AWP (AWPAI and AWPTI) seasonal cycles of NCAR-CCSM4, CSIRO-MK360, GISS-E2H, GISS-E2R, MOHC-HadCM3, MPI-ESM-LR, MPI-ESM-P have comparable amplitudes as ERSST. Though each individual model has changed or made no progress in simulating the AWP seasonal cycle compared with its corresponding previous generation model, the ensemble mean of AWP climatology in CMIP5 models is somewhat improved overall, as well as the model spreads decrease. However, the state-of-the-art CGCMs in CMIP5 still suffer from a significant cold bias in the AWP region.

b. Bias analysis

The AWP peaks in summer and fall. To compare with ERSST, the SST bias pattern is shown for the 19 member ensemble mean of CMIP5 (Figures 3.b.1-3.b.4) and for selected models (Figure 3.c-e). The ensemble mean character similar with CMIP3 (LWLE, 2012) as shown in 3.b.1-4 is that, in addition to the cold bias north of the equator, the southeast Atlantic

warm SST bias including the cold tongue and the Angola-Benguela coastal regions exists in all the models except CSIRO-MK3.6 (Figure 3.d.1-4) for all four seasons. It is possible that the positive feedback of wind, evaporation and SST (WES) which causes the tropical Atlantic Variability (Xie and Carton 2004) may generate these opposite biases across the equator. The process is that the warm bias in the southeast tropical Atlantic induces stronger Northeast Trade winds in the NTA, and then leads to more latent heat loss, therefore a cold SST bias of the NTA can be formed which in turn decreases the Southeast trade winds and enhances the warm bias in the southeast tropical Atlantic due to less latent heat loss. IPSL-CM5B-LR (Figure 3.e.1-4), similar with IPSL-CM5A-LR, IPSL-CM5A-MR and MR-CGCM3 (not shown), has a cold bias with maxima across the tropical North Atlantic, which resembles a strip and is located near 15° N. This character is different from the cold SST bias pattern of the NTA in the other CGCMs, which indicates that different mechanisms lead to the cold bias in the CGCMs.

Grodsky et al. (2012) found that the atmospheric component of CCSM4 has abnormally intense surface subtropical high pressure systems which cause the northeast trade winds to be too strong and lead to an excessively large latent heat loss in the NTA region. Before we examine this process here for the CMIP5 CGCMs, it should be noted that the cold SST bias enhances the SLP by raising the air density above it. In fact, the positive (negative) SLP bias (right panels in Figure 4.b.1-4) is largely collocated with the cold (warm) SST bias (Figure 3.b.1-4), which seems to support a strong effect (or feedback) of the SST bias on the SLP. Except GISS-E2H, GISS-E2R, HadCM3, the SLP bias pattern of 16 CGCMs shares the similarity with the ensemble as shown in Figure 4. The CGCMs can capture the major characters of SLP climatology (Figure 4.a.1-4), but in most of the NTA region, the CGCMs overestimate SLP by 2 hpa (Figure 4.b.1-4). In the northeast trade winds region of CGCMs ensemble (Figure 5.a.1-4), there is always a

positive wind speed bias throughout all the four seasons (Figure 5.b-1-4). The latent heat loss maximum centered to the south of Gulf Stream is mainly located in the AWP region (Figure 6.a.1-4). The latent heat loss bias in the AWP region is positive instead of negative as shown in the NTA region for the CGCMs ensemble (Figure 6.b.1-4). It suggests that for most models, the NTA cold SST bias can be traced to excessive evaporation due to erroneously high SLP and strong northeast trade winds. However, in the AWP region this mechanism is not able to explain the cold SST bias.

The pressure vertical velocity at 500mb of the CGCMs ensemble (Figure 7.a.1-4) shows the location of the ITCZ and its seasonal cycle. Compared with 20CR, CGCMs in the AWP region has subsidence bias all year round. This subsidence bias may be induced by overturning through the uplift process in the ITCZ of the east Pacific (Figure 7.b.1-4), since the convection over Amazonian region is also much weakened in CGCMs. The subsidence bias tends to suppress high level cloud formation and increase low level cloud formation. LWLE12 found that the negative SST bias of CMIP3 in the AWP region is connected with an excessive amount of simulated low-level cloud, which blocks shortwave radiation from reaching the sea surface. This positive feedback of colder SST, increased fraction of low level-cloud and decreased surface shortwave flux (Figure 9) may enhance the cold SST bias. However, it is uncertain to what extent the excessive simulated low-level clouds in CMIP3 CGCMs cause or are caused by the SST bias. The same analysis was performed on the output from CMIP5 CGCMs. We don’t find the relationship of higher AWP SST corresponding to more shortwave radiation and less low-level cloud fraction during AWP peak season. Higher AWP SST in ASO, however, corresponds to less net longwave heat loss (Figure 8.a), due to an increase in the downward longwave heat flux (Figure 8.b), and to more high-level cloud fraction among the CMIP5 CGCMs. This relationship

suggests that though there is still subsidence bias for the CMIP5 CGCMs in the AWP region, excessive high-level clouds are simulated (Jiang et al. 2012) and the warming effect of the high-level clouds radiative forcing (Su et al. 2008) as shown in Figure 9 dominates the modulation of AWP SST bias (the warming effect of the high-level clouds means that high-level clouds tend to reflect more longwave radiation back to earth surface and have less impact on downward shortwave radiation, and therefore have a warming effect on sea surface). Thus more (less) high-level clouds simulation may decrease (enhance) the cold AWP SST bias.

Why excessive high-level clouds are simulated compared with CMIP3? Significant improvements in both deep convection scheme and shallow convection scheme have been made in CMIP5. For example GFDL AM3 (Donner et al. 2011) includes new treatments of deep and shallow cumulus convection, cloud droplet activation by aerosols, subgrid variability of stratiform vertical velocities for droplet activation, and atmospheric chemistry driven by emissions with advective, convective, and turbulent transport. The other possible reason is that the mean state of AWP SST of CGCMs increases in CMIP5 though the cold SST bias still exists. In general lower SST tends to form more shallow convection and leads to more convection-related low-level clouds. Higher SST tends to induce more deep convection and then more high-level clouds can be formed. The increases of mean AWP SST in CMIP5 may also mitigate the excess low-level cloud formation and explain why low-level clouds and AWPTI are not correlated in CMIP5. Again the ultimate origin of the cold bias remains unknown.

4. AWP variability

a. Spectrum analysis

Power spectrum analyses of the time series of monthly AWPTI are shown in Figure 10.

There is significant energy at multidecadal periods between about 20 years and 32 years and longer than 32 years in ERSST (Figure 10.a). The spectrums of most CGCMs, however, demonstrate peaks in the interannual band (3-7 years), the decadal band (8-20 years) and the multidecadal band (20-30, 40-60 years or longer) all with 95% significance as shown in Figure 10.b. The ensemble spectra of the CGCMs also reflect the three bands. Based on the spectral character of the model ensemble, four groups of models are categorized as shown in Table 2. In Category I (as shown in Figure 10.c), four models simulate the significant multidecadal bands: GFDL-CM3, MOHC-HadGEM2CC, MPI-ESM-LR, MRI-CGCM3. In Category II (shown in Figure 10.d), three models simulate the interannual band and multidecal bands: GFDL-ESM2G, GFDL-ESM2M and MOHC-HadCM3 at the 95% significance level. In category III six models (Figure 10.e), consisting of GISS-E2H, GISS-E2R, INM-CM4, IPSL-CM5A-MR, MPI-ESM-P and NCC-NorESM1-M, simulate significant variability for the decadal and multidecadal bands. In category IV six models simulate significant variability for the interannual, decadal and multidecadal bands (Figure 10.f): CCCMA-CanESM2, NCAR-CCSM4, CSIRO-MK3.6.0, MOHC-HadGEM2ES, IPSL-CM5A-MR and IPSL-CM5B-LR. Because a higher SST anomaly leads to increase deep convection and the convection-related net heat flux tends to cool the AWP (Wu et al., 2006), this local air-sea interaction tends to damp AWP SST anomalies and decrease their interannual variability though the AWP still demonstrates substantial interannual variations through non-convection related processes such as advection. However, no significant periods are shown for the AWP interannual variability of the observations. The CGCMs are limited in their representation of the local air-sea interaction as discussed in Wu et al. (2006) and also show strong AWP internal variability with significant periods on the interannual band (LWLE12). The source of low-frequency variability on the multidecadal timescale is possibly from oceanic

processes (Delworth and Mann 2000).

In summary, spectrum analysis of ERSST reveals that multidecadal variability is dominant in the AWP region. It suggests that there is no significant period for interannual variability. It doesn't mean that the interannual variation is weak. On the contrary, the standard deviation of AWPTI on the interannual band for both observation and CGCMs is larger than the deviation on the longer time scales (Figure 11). 11 out of 19 CGCMs have larger standard deviation of AWPTI compared with observations. In the next two sections, we focus on the interannual and multidecadal variability of the AWP in its peak season.

b. Interannual variability

We perform rEOF analysis on the tropical Atlantic ASO SST from 30˚S to 30˚N as shown in Figure 10. The first mode of observations with 17.0% variance (Fig. 12.a.1) is a STA-EQ mode featuring maximum SST anomalies on the equator and associated changes in the easterly trade winds (Philander 1986; Zebiak 1993; Carton and Huang 1994). The second mode is the NTA mode with 13.0% variance (Fig. 12.a.2). The SST anomalies are centered near African coast in the northern tropical Atlantic Ocean. The third mode is the STA-BQ mode with 10.3% variance characterized by SST fluctuations centered along the Benguela coast. The fourth mode is SSA mode with 10.2% variance featuring maximum SST anomalies in the open ocean of the subtropical Atlantic. AWP interannual variability is primarily dominated by these four modes though the variance of these modes in the AWP region is small.

The rEOF modes of CGCMs are listed in Table 2. Compared with the rEOF modes of ERSST, the CGCMs are categorized into three groups. Category I, consisting of NCAR-CCSM4 (Figure 12.b.1-4) and GISS-E2H (Figure 12.c.1-4), successfully captures all the first four modes

of observations with the overall character of each mode. Category II, consisting of CCCMA-CanESM2, CSIRO-MK360, GISS-E2R, MOHC-HadGEM2-ES, INM-CM4, IPSL-CM5A-LR, IPSL-CM5A-MR, IPSL-CM5B-LR and MRI-CGCM3 (Figure 12.d.1-4), is able to simulate the SSA, NTA and STA in their first four modes. In this group CGCMs, however, can't separate STA-EQ and STA-BG modes. A different type of NTA mode across the basin as shown in Figure 12.d.1 is captured by many CMIP5 CGCMs and we defined it as NTA II mode. Huang et al. (2004) pointed out that this mode is likely stronger in boreal summer in the tropical Atlantic and seems to be associated with the tropical extension of the midlatitude SST anomalies as the "North Atlantic Horse shoe" pattern. This pattern also resembles the remote forced pattern in NTA by ENSO and the NAO (Czaja and Marshall 2001). As we will discuss the remote connection in section 4.d, we find that for some CGCMs the influences of the NAO and/or ENSO can last from boreal spring to summer as shown in Figure 14.e.1-2. This overestimated remote forced pattern in summer can be embedded into tropical Atlantic variability and here we ascribe remote forcing to the cause of NTA II mode of CGCMs. Category III, consisting of GFDL-CM3, GFDL-ESM2G, GFDL-ESM2M, MOHC-HadCM3, MOHC-HadGEM2, MPI-ESM-LR, MPI-ESM-P and NCC-NorES1-M, can only capture two modes of the first four ERSST modes. The patterns which cannot be defined as any one of the four modes of ERSST are not discussed and listed in Table 2. Those patterns may be related with model bias.

c. Multidecadal variability

Based on the AWPTI of ERSST, the pattern of global SST difference between large AWP years and small AWP years on the multidecadal timescale is shown in Figure 13.a. The threshold value of AWPTI to define large (small) AWP years is 0.1^{o}C (-0.1^{o}C). As discussed by LWLE12,

this pattern is identical to the pattern regressed on AWPAI of JJASO (Wang et al. 2008a), but also has global warming signature included because the linear detrending cannot remove the entire global warming signal. The spatial pattern suggests that the AWP multidecadal variability resembles the AMO, which is well supported by a close relationship between the AWPTI and AMO index. For the ensemble of 19 models, the pattern of global SST difference between large AWP years and small AWP years shown in Figure 13.b has a realistic representation of the observed AMO pattern. Compared with ERSST, 14 models: CanESM2, CSIRO-MK360, GFDL-CM3 (Figure 13.d), GFDL-ESM2G, GISS-E2H, GISS-E2R, HadGEM2CC, INMCM4, IPSL-CM5A-LR, IPSL-CM5A-MR, IPSL-CM5B-LR, MPI-ESM-LR, MPI-ESM-P and NorESM1, successfully reproduce the major characteristics of the observed pattern of global SST difference between large AWP years and small AWP years. NCAR-CCSM4 (Figure 13.c), GFDL-ESM2M and MRI-CGCM3 show a global warming signature with out-of-phase cooling to the south of Greenland Island. MOHC-HadCM3 and MOHC-HadGEM2ES have significant cooling pattern in the north Pacific instead of warming shown in most CGCMs.

d. Remote connection

Next we focus on the interannual variability of the AWP induced by remote influences. AWP variability can be remotely influenced by ENSO and the NAO. Czaja et al. (2002) and Enfield et al. (2006) studied the delayed influence of ENSO and the NAO on the tropical North Atlantic region. Here we performed the same analysis as LWLE12 on the AWP region to show how this remote influence acts on the AWP in CGCMs. We regress zonally averaged observed variables including surface wind stress, net surface heat flux and SST in the AWP region on the Niño-3 SST index (Fig. 14.a.1) and the negative NAO index (Fig. 14.a.2) from January to

December. Figure 14.a.1 shows that positive ENSO events correspond to westerly low-level wind anomalies over the AWP (shown in vectors) which are largest during JFM. This wind anomaly induces heating between 5˚N and 20˚N over the AWP region at a rate of 8 W m^{-2} due to a decreased latent heat loss (shown in contour) and leads to a warm SST anomaly (shown in shading) of 0.2˚C during FMAM. Figure 14.a.2 shows a regression pattern on the negative NAO index similar to Figure 14.a.1. But the magnitude of the SST warming anomaly between 5˚N and 20˚N is about 0.2˚C less than the magnitude of ENSO influence. The anomalous net heat flux also switches sign after March. The same results have been addressed in detail in LWLE12. The mechanism determining the forcing of AWP variability in spring by both ENSO and the NAO is similar with the mechanism suggested by Czaja et al. (2002) for the NTA.

Compared with the above observational analysis, the ensemble of the 19 analyzed models successfully simulates the observed remote influence pattern in the AWP region induced by both ENSO (Fig. 14.b.1) and the NAO (Fig. 14.b.2). Only four models, identified as Category I, are able to successfully capture the major features for the remote influence from both the ENSO and NAO influences: NCAR-CCSM4 (Figure 14.c.1-2), GISS-E2H, GISS-E2R and NCC-NorESM1M. Four models in Category II are able to capture the major character of the NAO influence: MOHC-HadGEM2CC (Figure 14.d.1-2), MOHC-HadGEM2ES, INM-CM4, IPSL-CM5A-MR. In these models, the wind-evaporation-SST mechanism still holds valid in explaining the processes. However, the process of warming in FMAM between 5˚N and 20˚N induced by ENSO is not captured or captured but lasts to ASO. Category III, consisting of CCCMA-CanESM2, CSIRO-MK360, GFDL-CM3, GFDL-ESM2G, GFDL-ESM2M, MOHC-HadCM3, IPSL-CM5A-LR, IPSL-CM5B-LR, MPI-ESM-LR, MPI-ESM-P and MRI-CGCM3 (Figure 14.e.2), is not able to successfully simulate the observed regression patterns for both

ENSO and the NAO. These models either simulated a delayed warming in ASO pattern (Figure 14.e.2) or are even not able to capture the warming phase between 5˚N and 20˚N compared with observations.

In Figure 15.a, a Taylor diagram is constructed using the regression coefficients of ENSO influence shown in Figure 14 to quantify the performance of CGCMs. The correlation between each model and observations is calculated between the regression coefficient at each grid point of model and the regression coefficient at the same grid points of observation as shown in the domain of Figure 14.a.1. The standard deviation for the statistics of each model is divided by the standard deviation of observations. The reference point “A” for perfect correspondence of models to observations is at the (1, 1) point of standard deviation and correlation coefficient coordinates. If the point of a model in the diagram is closer to the reference point, then the model has a better performance in representing the observed pattern.

By this metric NCAR-CCSM4 (C), INM-CM4 (M), GISS-E2H (H), NCC-NorESM1M (T) are the models that best replicate the AWP connection to ENSO. Except INM-CM4, all the other three models are categorized as the best models in earlier discussion in simulating ENSO influence on the AWP based on subjective judgment. For INM-CM4, the regression pattern of ENSO has notable erroneous warming close to the equator, except the warming between 5˚N and 20˚N in spring as in observations. So we regard this model as the one unable to simulate the ENSO influence successfully. In general, the Taylor diagram has proved to be successful tool to quantitatively evaluate the performance of CGCMs.

Figure 15.b is the same as Figure 15.a except that the statistics are defined as regression coefficients of SST onto the NAO (DJFM) index at all grid points within the domain as shown in Figure 14.a.2. GISS-E2H (H) and MPI-ESM-P (Q) are the best two models compared with the

reference point for observations. MPI-ESM-P, however, has a delayed NAO influence till ASO, so it is not summarized as one of the best model in simulating NAO influence in earlier discussion. Comparison between Figure 15.a and Figure 15.b indicates that the selected 19 CMIP5 CGCMs, unlike the CGCMs in CMIP3, demonstrate a comparable performance in simulating remote influence pattern in the AWP region induced by the NAO with the performance in simulating the influence induced by ENSO. This conclusion is also reflected in the regression patterns of the model ensemble mean in Figure 14.b.1 and Figure 14.b.2.

5. Summary and Discussion

In this paper we explore AWP variability in 19 CGCMs from the CMIP5 database and validate them against observations over the twentieth century at the seasonal, interannual and multidecadal time scales, as well as for the remote connections with ENSO and the NAO. Both the AWPAI and AWPTI are defined to study the seasonal cycle. Severn models, NCAR-CCSM4, CSIRO-MK360, GISS-E2H, GISS-E2R, MOHC-HadCM3, MPI-ESM-LR and MPI-ESM-P have the best performance in simulating the AWP seasonal cycle based on both indexes. The AWPAI is almost zero for some models in most years due to cold SST bias found in the northern tropics for most models. Thus, we have chosen an SST index as a more effective but equivalent proxy for AWP variability. Only NCAR-CCSM4 and GISS-E2H are able to capture all the first four modes of ERSST rEOF. Analysis of the AWP remote connection with ENSO and the NAO shows that NCAR-CCSM4, GISS-E2H, GISS-E2R and NCC-NorESM1M are the best group of models in simulating the processes by which ENSO and NAO influence the AWP region through wind-evaporation-SST interactions. 14 models listed in Table 3 successfully capture the spatial characters of global SST between large AWP years and small AWP years. All the best models in

each evaluation aspect are summarized in Table 3. NCAR-CCSM4, GISS-E2H and GISS-E2R are best models in simulating the AWP variability based on this study. The previous generation of models developed at NCAR and GISS (CCSM3, GISSer and GISSaom) are quite limited in AWP simulation (LWLE12) and hence are much improved in their CMIP5 reincarnation. As the physics and configuration for every CGCM are improved and more complex compared with CMIP3 CGCMs, the results presented in this study provide a useful reference in continuing to improve CGCM simulations of the AWP.

As discussed with respect to the AWP seasonal cycle, the cold SST bias in the AWP region still exists in most CMIP5 CGCMs. The pattern of the warm SST bias in the cold tongue and Angola-Namibia region and cold bias in the NTA is a ubiquitous feature of most CGCMs from both CMIP3 and CMIP5. The analysis of NTA SST bias in the study of Grodsky et al. (2012) showed that the atmospheric components of CCSM3 and CCSM4 have abnormally intense subtropical high pressure systems and abnormally weak subpolar low pressure systems, and these SLP biases cause excessively strong surface winds and result in too large latent heat loss and cold SST bias throughout the NTA basin. We examine this process among 19 CGCMs of CMIP5 and we find that excessively strong subtropical highs are able to explain the cold SST bias in the NTA region for most CGCMs. However, a positive bias in the North Atlantic subtropical high (NASH) is unable to explain the cold SST bias in the AWP region because the excess latent heat loss is much smaller compared with observations possibly due to weaker sea surface specific humidity gradient. We adopt the same latent heat flux dataset（IFREMER) used in Grodsky et al. (2012) as observation reference instead of the latent heat flux data from 20CR for consistency. However, if we use the latent heat flux data of 20CR and NCEP reanalysis datasets as reference, the excess latent heat loss is also much smaller in the AWP region (Figures

are not shown) and our conclusion is consistency for these different datasets.

We find that among the CGCMs of CMIP5, SST is positively correlated with high-level cloud fraction and downward longwave radiation in the AWP region. It indicates that lower (higher) AWP SST contributes to less (more) high-level cloud fraction and thus leads to less (more) reflected downward longwave radiation. The decreased (increased) longwave radiation can further decrease (warm) the AWP SST. This positive feedback may erroneously alleviate the AWP SST cold bias when excessively high-level clouds are simulated. The origin of the cold bias in the AWP is still uncertain. A recently published paper of Fasullo and Trenberth (2012) suggests that the present models with low climate sensitivity perform more inadequately in replicating climate teleconnections between the tropics and subtropics, and are identifiably biased. They pointed out that the relative contributions of various cloud types to the overall cloud feebback and the sources of biases in the vertical relative humidity and cloud distributions in models are two of major questions to be solved for correctly simulating climate sensitivity. These two questions may also be of fundamental importance to trace the origin of the topical SST bias in models.

Acknowledgement: We acknowledge the World Climate Research Programme's Working Group on Coupled Modelling, which is responsible for CMIP, and we thank the climate modeling groups (listed in Table 1 of this paper) for producing and making available their model output. For CMIP the U.S. Department of Energy's Program for Climate Model Diagnosis and Intercomparison provides coordinating support and led development of software infrastructure in partnership with the Global Organization for Earth System Science Portals. This work was supported by grants from the National Oceanic and Atmospheric Administration’s Climate

Program Office and by grants from the National Science Foundation.

References

Bell, G. D., and M. Chelliah, 2006: Leading tropical modes associated with interannual and multi-decadal fluctuations in North Atlantic hurricane activity. *J. Climate*, **19**, 590–612.

Carton, J. A., and B. H. Huang, 1994: Warm events in the tropical Atlantic, *J. Phys. Oceanogr*., **24**, 888–903.

Chang, C.-Y., J. A. Carton, S. A. Grodsky, and S. Nigam, 2007: Seasonal climate of the tropical Atlantic sector in the NCAR Community Climate System Model 3: Error structure and probable causes of errors. *J. Climate*, **20**, 1053-1070.

Chang, C.-Y., S. Nigam, and J.A. Carton, 2008: Origin of the Spring-time Westerly Bias in Equatorial Atlantic Surface Winds in CAM3/CCSM3 Model Simulations, *J. Clim*., **21**, 4766-4778.

Chang, P., L. Ji and H. Li, 1997: A decadal climate variation in the tropical Atlantic ocean from thermodynamic air-sea interactions. *Nature*, **385**, 516-518.

Clement, A. C., R. Burgman, and J. R. Norris, 2009: Observational and model evidence for positive low-level cloud feedback. *Science*, **325**, 460-464.

Compo, G.P., J.S. Whitaker, P.D. Sardeshmukh, N. Matsui, R.J. Allan, X. Yin, B.E. Gleason, R.S. Vose, G. Rutledge, P. Bessemoulin, S. Brönnimann, M. Brunet, R.I. Crouthamel, A.N. Grant, P.Y. Groisman, P.D. Jones, M. Kruk, A.C. Kruger, G.J. Marshall, M. Maugeri, H.Y. Mok, Ø. Nordli, T.F. Ross, R.M. Trigo, X.L. Wang, S.D. Woodruff, and S.J. Worley, 2011: The Twentieth Century Reanalysis Project. *Quarterly J. Roy. Meteorol. Soc*., **137**, 1-28. doi: 10.1002/qj.776.

Czaja, A., and J. Marshall, 2001: Observations of atmosphere–ocean coupling in the North Atlantic. *Quart. J. Roy. Meteor. Soc*., **127**, 1893–1916.

Czaja, A., P. van der Vaart, J. Marshall, 2002: A Diagnostic Study of the Role of Remote Forcing in Tropical Atlantic Variability. *J. Climate*, **15**, 3280–3290. doi: 10.1175/1520-0442(2002)015<3280:ADSOTR>2.0.CO;2

de Szoeke, S. P., and S.-P. Xie, 2008: The tropical eastern Pacific seasonal cycle: Assessment of errors and mechanisms in IPCC AR4 coupled ocean–atmosphere general circulation models. *J. Climate*, **21**, 2573–2590.

Delworth, T. L., and M. E. Mann, 2000: Observed and simulated multidecadal variability in the Northern Hemisphere. *Clim. Dyn*., **16**, 661–676.

Donner, Leo J., and Coauthors, 2011: The Dynamical Core, Physical Parameterizations, and Basic Simulation Characteristics of the Atmospheric Component AM3 of the GFDL Global

Coupled Model CM3. *J. Climate*, **24**, 3484–3519.doi: http://dx.doi.org/10.1175/2011JCLI3955.1

Doi, T., T. Tozuka, and T. Yamagata, 2010: The Atlantic meridional mode and its coupled variability with the Guinea Dome. *J. Climate*, **23**, 455-475.

Enfield, D. B., and D. A. Mayer, 1997: Tropical Atlantic sea surface temperature variability and its relation to El Nin˜o–Southern Oscillation. *J. Geophys. Res*., **102**, 929–945.

Enfield, D. B., A. M. Mestas-Nuñez, D. A. Mayer, and L. Cid-Serrano, 1999: How ubiquitous is the dipole relationship in tropical Atlantic sea surface temperatures*?, J. Geophys. Res*., **104**(C4), 7841–7848, doi:10.1029/1998JC900109.

Enfield, D. B., A. M. Mestas-Nuñez, and P. J. Trimble, 2001: The Atlantic Multidecadal Oscillation and its relation to rainfall and river flows in the continental U.S., *Geophys. Res. Lett*., **28**(10), 2077-2080.

Enfield, D. B., S.-K. Lee, 2005: The Heat Balance of the Western Hemisphere Warm Pool. *J. Climate*, **18**, 2662-2681.

Enfield D.B., S.-K. Lee, and C. Wang, 2006: How are large Western Hemisphere Warm Pools formed? *Progress in Oceanography*, **70**(2-4), 346-365.

Enfield, D.B., and L. Cid-Serrano, 2009: Secular and multidecadal warmings in the North Atlantic and their relationships with major hurricane activity. *International Journal of Climatology.* **30**(2):174-184, doi:10.1002/joc.1881.

Fasullo,T.T., and K. E. Trenberth, 2012: A Less Cloudy Future: The Role of Subtropical Subsidence in Climate Sensitivity. *Science* **338**, 792 (2012).

Gordon, H, Siobhan O'Farrell, Mark Collier, Martin Dix, Leon Rotstayn, Eva Kowalczyk, Tony Hirst and Ian Watterson, 2010: The CSIRO Mk3.5 Climate Model, CAWCR Technical Report No. **021**.

Grodsky, S. A., J. A. Carton, S. Nigam, Y. M. Okumura, 2012: Tropical atlantic biases in ccsm4. *J. Climate*, **25**, 3684–3701. doi: http://dx.doi.org/10.1175/JCLI-D-11-00315.1.

Hu, Z.-Z., B. Huang, and K. Pegion, 2008: Leading patterns of the tropical Atlantic variability in a coupled general circulation model. *Climate Dyn*., **30**, 703-726.

Huang, B., P. S. Schopf, J. Shukla, 2004: Intrinsic ocean–atmosphere variability of the tropical atlantic ocean. *J. Climate*, **17**, 2058–2077. doi: http://dx.doi.org/10.1175/1520-0442(2004)017<2058:IOVOTT>2.0.CO;2.

Huang, B, J. Shukla, 2005: Ocean–atmosphere interactions in the tropical and subtropical atlantic ocean. *J. Climate*, **18**, 1652–1672. doi: http://dx.doi.org/10.1175/JCLI3368.1.

Hurrell, J. W., 1995: Decadal trends in the North Atlantic Oscillation: regional temperatures and precipitation. *Science*, **269**, 676-679.

Jiang, J. H., et al. 2012: Evaluation of cloud and water vapor simulations in CMIP5 climate models using NASA "A-Train" satellite observations, *J. Geophys. Res*., **117**, D14105, doi:10.1029/2011JD017237.

Joseph, R., and S. Nigam, 2006: ENSO Evolution and Teleconnections in IPCC's 20th Century Climate Simulations: Realistic Representation? *J. Climate*, **19**, 4360-4377.

Large, W. G., G. Danabasoglu, 2006: Attribution and impacts of upper-ocean biases in ccsm3. *J. Climate*, **19**, 2325–2346. doi: http://dx.doi.org/10.1175/JCLI3740.1.

Latif, M. and A. Grötzner, 2000: On the equatorial Atlantic oscillation and its response to ENSO. *Clim. Dyn*., **16**, 213-218.

Liu, H., C. Wang, S. Lee, and D. Enfield, 2012: Atlantic Warm Pool Variability in the IPCC-AR4 CGCM Simulations. *J. Climate*. doi:10.1175/JCLI-D-11-00376.1.

Lee, S.-K., D. B. Enfield and C. Wang, 2007: What Drives Seasonal Onset and Decay of the Western Hemisphere Warm Pool? *J. Climate*, **20**, 2133-2146.

Lee, S.-K., D. B. Enfield, C. Wang, 2008: Why do some El Ninos have no impact on tropical North Atlantic SST? *Geophys Res. Let*., **35**, L16705.

Li, G. and S.-P. Xie, 2012: Origins of tropical-wide SST biases in CMIP multi-model ensembles, Geophys. Res. Lett., 39, L22703, doi:10.1029/2012GL053777.

Meehl, G.A., C. Covey., K. E. Taylor, T. Delworth, R. J. Stouffer, M. Latif, B. McAvaney, J. F. B. Mitchell, 2007: The WCRP CMIP3 multimodel dataset: a new era in climate change research. *Bull. Amer. Meteor. Soc*., **88**, 1383–1394.
doi: http://dx.doi.org/10.1175/BAMS-88-9-1383.

Miller, R. L., et al. 2006: Mineral dust aerosols in the NASA Goddard Institute for Space Sciences ModelE atmospheric general circulation model, *J. Geophys. Res*., **111**, D06208, doi:10.1029/2005JD005796.

Vasubandhu, M., S. Chan, R. Wu, and E. Chassignet, 2009: Air-sea interaction over the Atlantic warm pool in the NCEP CFS. *Geophys. Res. Lett*., **36**, L15702, doi:10.1029/2009GL038525.

Muñoz, E., W. Weijer, S. A. Grodsky, S. C. Bates, I. Wainer, 2012: Mean and variability of the tropical atlantic ocean in the ccsm4*. *J. Climate*, **25**, 4860–4882. doi: http://dx.doi.org/10.1175/JCLI-D-11-00294.1.

Nobre, P., and J. Shukla, 1996: Variations in sea surface temperature, wind stress, and rainfall

over the tropical Atlantic and South America. *J. Climate*, **9**, 2464–2479.

Okumura, Y., and S.-P. Xie, 2006: Some overlooked features of tropical Atlantic climate leading to a new Nino-like phenomenon. *J. Climate*, **19**, 5859-5874.

Philander, S. G. H., Predictability of El Nino, 1986: *Nature*, **321**, 810-811.

Richter I, Xie S-P ,2008: On the origin of equatorial Atlantic biases in coupled general circulation models. *Clim Dyn* **31**:587–598.

Richter I, S.-P. Xie, A. T. Wittenberg, and Y. Masumoto, 2012: Tropical Atlantic biases and their relation to surface wind stress and terrestrial precipitation. *Climate Dyn*., doi:10.1007/s00382-011-1038-9.

Saji, N. H., S.-P. Xie, and T. Yamagata, 2006: Tropical Indian Ocean variability in the IPCC 20th-century climate simulations. *J. Climate*, **19**, 4397-4417.

Setvain, J., 1991: Simple climate indices for the tropical Atlantic Ocean and some applications, *J. Geophys. Res.*, **96**, 15137-15146.

Smith, T.M., R.W. Reynolds, Thomas C. Peterson, and Jay Lawrimore, 2008: Improvements to NOAA's Historical Merged Land-Ocean Surface Temperature Analysis (1880-2006). *J. Climate*, **21**, 2283-2296.

Su, H., et al. 2008: Variations of tropical upper tropospheric clouds with sea surface temperature and implications for radiative effects, *J. Geophys. Res.*, **113**, D10211, doi:10.1029/2007JD009624.

Taylor, K. E., 2001: Summarizing multiple aspects of model performance in a single diagram, *J. Geophys. Res*., **106**, 7183–7192, doi:10.1029/2000JD900719.

Torrence, C. and G. P. Compo, 1998: A practical guide to wavelet analysis. *Bull. Amer. Meteor. Soc*., **79**, 61-78.

Tozuka, T. Doi, T. Miyasaka, N. Keenlyside, and T. Yamagata, 2011: How to simulate the equatorial Atlantic zonal SST gradient realistically in a coupled GCM. *J. Geophys. Res*., **116**, C06010, doi:10.1029/2010JC006717.

Xie, S.-P., Y. Tanimoto, H. Noguchi, and T. Matsuno, 1999: How and why climate variability differs between the tropical Atlantic and Pacific, *Geophys. Res. Lett*., **26**, 1609– 1612, doi:10.1029/1999GL900308.

Xie, S.-P., and J.A. Carton, 2004: Tropical Atlantic variability: patterns, mechanisms, and impacts, in “Ocean-Atmosphere Interaction and Climate Variability”, edited by C. Wang, S.-P. Xie, and J. A. Carton, AGU Press.

Wang, C., and D.B. Enfield, 2001: The tropical Western Hemisphere warm pool. *Geophys. Res. Lett*, **28**, 1635-1638.

Wang, C., and D.B. Enfield, 2003: A further study of the tropical Western Hemisphere warm pool. *J. Climate*, **16**, 1476-1493.

Wang, C., D.B. Enfield, S.-K. Lee, and C.W. Landsea, 2006: Influences of the Atlantic warm pool on Western Hemisphere summer rainfall and Atlantic hurricanes. *J. Climate*, **19**, 3011-3028.

Wang, C., S.-K. Lee, and D. B. Enfield, 2008a: Atlantic warm pool acting as a link between Atlantic multidecadal oscillation and Atlantic tropical cyclone activity. *Geochem. Geophys. Geosyst*., **9**, Q05V03, doi:10.1029/2007GC001809.

Wang, C., S.-K. Lee, and D. B. Enfield, 2008b: Climate response to anomalously large and small Atlantic warm pools during the summer. *J. Climate*, **21**, 2437-2450.

Wang, C., H. Liu, S.-K. Lee, and R. Atlas, 2011: Impact of the Atlantic warm pool on United States landfalling hurricanes, *Geophys. Res. Lett*., **38**, L19702, doi:10.1029/2011GL049265.

Wang, X., D. Wang, and W. Zhou, 2009: Decadal variability of twentieth century El Niño and La Niña occurrence from observations and IPCC AR4 coupled models, *Geophys.Res. Lett*., **36**, L11701, doi: 10.1029/2009GL037929.

Wu, R.G., B. P. Kirtman, K. Pegion, 2006: Local Air–Sea Relationship in Observations and Model Simulations. *J. Climate*, **19**, 4914–4932.

Zebiak, S. E., 1993: Air-sea interaction in the equatorial Atlantic region, *J. Climate*, **6**, 1567–1586.

List of Tables

Table 1. The 19 models of CMIP5 involved in this study and their development institutions, letter denotations, short names used throughout the paper, and time periods of historical simulations. CMIP3 models are also listed by institutions for reference.

Table. 2 First four rEOF modes of ERSST and CGCMs with their variances.

Table 3. Summary of best performance models in each aspect of variability evaluation.

List of Figures

Figure 1 Climatology of (a) AWPAI, (b) AWPTI, AWP box averaged (c) net surface heat flux of 20CR, (d) net surface heat flux of CMIP5 minus CMIP3, (e) net surface heat flux of CMIP5 minus 20CR, (f) net surface heat flux of CMIP3 minus 20CR. Positive value of heat fluxes mean ocean gains heat. AWP box is defined within 5^0N-30^0N and land-40^0W. Black line with circle is for ERSST in (a). Blue line is ensemble of CMIP5 CGCMs. Grey dash is ensemble of CMIP3 models. Model spreads are represented by vertical bars. Black dashed line in (d), (e) and (f) stands for AWPTI*10 in ^{o}C.

Figure 2 AWP box averaged net surface heat flux bias and AWPTI bias for selected models: (a) GISSE2R_CMIP5, (b) GISSER_CMIP3, (c) CCSM4_CMIP5, (d) CCSM3_CMIP3, (e) GFDLCM3_CMIP5, (f) GFDLCM2_CMIP3, and (g) CSIRO36_CMIP5. Heat flux bias is in Unit W/m^2. AWPTI is in Unit ^{o}C.

Figure 3 Observational SST and model SST bias in four seasons. Shown are (a1-a4) ERSST SST averaged in four seasons, (b1-b4) the seasonal SST bias of the 19 model ensemble, and (c1-c4, d1-d4, e1-e4) the seasonal SST bias for selected models. Unit is °C.

Figure 4 Climatology of SLP and model ensemble bias. (a1-4) are climatology of SLP. Shading stands for model ensemble. Contour lines stand for 20CR. (b1-4) are model ensemble bias for four seasons compared with 20CR. Unit is hPa.

Figure 5 Climatology of surface winds and model ensemble bias. (a1-4) are climatology of surface winds. Shading stands for wind speed of model ensemble. Vectors stand for wind vectors of model ensemble. Contour lines stand for wind speed of IFREMER data. (b1-4) are model ensemble bias for four seasons compared with IFREMER data. Shading stands for wind speed bias and vectors stand for wind vector bias. Unit is m/s.

Figure 6 Climatology of latent heat flux and model ensemble bias. (a1-4) are climatology of latent heat flux. Shading stands for model ensemble. Contour lines stand for IFREMER data. (b1-4) are model ensemble bias for four seasons compared with IFREMER data. Unit is W/m^2.

Figure 7 Climatology of pressure vertical velocity and model ensemble bias. (a1-4) are climatology of pressure vertical velocity. Shading stands for model ensemble. Contour lines stand for 20CR. (b1-4) are model ensemble bias for four seasons compared with 20CR.The sign of pressure vertical velocity is reversed and subsidence corresponds to negative pressure velocity. Unit is Pa/s.

Figure 8 Multi-model scatter plot in JASO of (a) net longwave radiation vs. AWPTI, (b) downward longwave radiation vs. AWPTI, and (c) high level cloud fraction vs. AWPTI. Each point stands for one model. The black line shows the least squares

linear fit to all points.

Figure 9 Diagram of different radiative properties of low and high level clouds and their associated feedback with SST in the AWP region..

Figure 10 Spectrum analysis of AWPTI. (a) spectrum of ERSST. Y axis is power. X axis is the wavelet period in years. The dashed line indicates 95% significance level. (b) (c), (d) and (e) are the same as (a) for the ensemble of 19 models with each model shown in grey line, Group I, Group II, Group III and VI models respectively.

Figure 11 AWPTI standard deviation of observations and CGCMs. Blue bar shows interannual band. Red bar shows decadal and longer time scale band.

Figure 12 rEOF analysis of tropical Atlantic SST in ASO months. Shown are (a1) first mode, (a2) second mode, (a3) third mode and (a4) fourth mode of ERSST. Same as (a1-4), (b1-4) are for NCAR-CCSM4, (c1-4) are for GISS-E2H, (d1-4) are for MRI-CGCM3.

Figure 13 Pattern of global SST difference between large AWP years and small AWP years on the decadal timescale and above. Shown are (a) ERSST, (b) ensemble of 19 models, (c) NCAR-CCSM4 and (d) GFDL-CM3. Unit is oC. The threshold value of AWPTI to define large (small) AWP years is 0.1^{o}C (-0.1^{o}C).

Figure 14 Regression map of surface wind stress (vector, N/m^2), net surface heat flux (positive into the ocean with solid contour line, W/m^2), and SST (shading contour, ^{o}C) averaged in longitude onto Niño-3 Index (DJF) and onto negative NAO index (DJFM). Shown are (a1) regression map onto Niño-3 Index for observations, (a2) regression map onto negative NAO Index for observations, (b1) regression map onto Niño-3 Index for ensemble of 19 models, (b2) regression map onto negative NAO Index for ensemble, (c), (d) and (e) are the same as (b) for selected models.

Figure 15 (a) A Taylor diagram of statistics describing the remote influenced patterns of ENSO on AWP in CGCMs as shown in Figure 14.a.1. On this diagram, the radial co-ordinate gives the magnitude of total standard deviation of lag regression coefficients in the domain of Figure 14.a.1 for each model normalized by the standard deviation of observation, and the angular co-ordinate gives the correlation of the regression coefficients of each model with the regression coefficients of observation. The distance between the reference point “A” of observation and any model's point (B to T defined in Table 1) is proportional to the root mean square error shown by the green dashed lines. (b) Same as (a), but the statistics of Taylor diagram describing the remote influenced patterns of NAO on AWP in CGCMs as shown in Figure 14.a.2.

Table 1. The 19 models of CMIP5 involved in this study and their development institutions, letter denotations, short names used throughout the paper, and time periods of historical simulations. CMIP3 models are also listed by institutions for reference.

Institution	Letter denotation	Abbreviation	Historical Run	CMIP3 model names defined in LWLE12
Canadian Centre for Climate Modelling and Analysis, Canada	B	CCCMA-CanESM2	1850-2005	CGCMt47, CGCMt63
National Center for Atmospheric Research, USA	C	NCAR-CCSM4	1850-2005	CCSM3, Npcm1
CSIRO (Commonwealth Scientific and Industrial Research Organisation, Australia), and BOM (Bureau of Meteorology, Australia)	D	CSIRO-MK3.6.0	1850-2005	CSIRO30, CSIRO35
Geophysical Fluid Dynamics Laboratory, USA	E	GFDL-CM3	1860-2005	GFDL20, GFDL21
	F	GFDL-ESM2G	1861-2005	
	G	GFDL-ESM2M	1861-2005	
NASA Goddard Institute for Space Studies, USA	H	GISS-E2H	1850-2005	GISSaom, GISSer
	I	GISS-E2R	1850-2005	
Met Office Hadley Centre, United Kingdom	J	MOHC-HadCM3	1859-2005	Uhadcm3, Uhadgem1
	K	MOHC-HadGEM2-CC	1859-2005	
	L	MOHC-HadGEM2-ES	1859-2005	
Institute for Numerical Mathematics, Russia	M	INM-CM4	1850-2005	INMCM3
Institut Pierre Simon Laplace, France	N	IPSL-CM5A-LR	1850-2005	IPSL
	O	IPSL-CM5A-MR	1850-2005	
	P	IPSL-CM5B-LR	1850-2005	
Max Planck Institute for Meteorology (MPI-M), Germany	Q	MPI-ESM-LR	1850-2005	MPI
	R	MPI-ESM-P	1850-2005	
Meteorological Research Institute, Japan	S	MRI-CGCM3	1850-2005	MRI
Norwegian Climate Centre , Norway	T	NCC-NorESM1M	1850-2005	

*Letter A stands for observations.

Table. 2 First four rEOF modes of ERSST and CGCMs with their variances.

Obs. and models	REOF1	REOF2	rEOF3	rEOF4
ERSST	STA-EQ: 17.0	NTA: 13.0	STA-BG: 10.3	SSA: 10.2
CCCMA-CanESM2	SSA: 20.0	NTA: 14.1	STA: 13.3	NTAII: 9.7
NCAR-CCSM4*	STA-EQ: 24.4	SSA: 12.4	STA-BG: 10.1	NTA: 10.0
CSIRO-MK3.6.0	NTAII: 21.3	NTA: 15.3	SSA: 13.5	STA: 11.0
GFDL-CM3	STA: 34.4	NTA: 10.7	\: 9.0	\: 8.5
GFDL-ESM2G	STA: 20.6	NTA: 13.6	NTAII: 10.1	\: 10.1
GFDL-ESM2M	STA-EQ: 35.4	\: 13.0	NTA: 9.6	STA-BG: 6.7
GISS-E2H*	STA-BG: 20.6	NTA: 15.6	STA-EQ: 13.9	SSA: 8.6
GISS-E2R	STA-BG: 20.0	NTAII: 12.4	NTA: 11.2	SSA: 10.9
MOHC-HadCM3	NTA: 15.9	\: 14.3	NTAII: 13.2	STA: 12.1
MOHC-HadGEM2-CC	NTA: 19.3	STA: 19.2	\: 8.6	\: 7.5
MOHC-HadGEM2-ES	NTA: 20.6	STA: 18.4	\: 8.1	SSA: 4.9
INM-CM4	STA: 15.4	NTA: 11.2	SSA: 8.8	\: 7.4
IPSL-CM5A-LR	NTA: 22.4	STA: 20.5	NTAII: 13.7	SSA: 12.3
IPSL-CM5A-MR	NTA: 24.2	STA: 17.0	SSA: 13.3	NTAII: 10.3
IPSL-CM5B-LR	NTA: 41.8	NTAII: 9.9	STA: 9.2	SSA: 5.7
MPI-ESM-LR	STA: 17.4	\: 17.3	NTA: 13.0	NTAII: 7.9
MPI-ESM-P	STA: 19.4	NTA: 11.7	\: 10.8	NTAII: 6.9
MRI-CGCM3	NTAII: 15.9	STA: 13.5	NTA: 10.7	SSA: 6.8
NCC-NorESM1M	STA-EQ: 27.5	\: 14.9	STA-BG: 10.2	NTAII: 8.5

STA: southern tropical Atlantic mode. NTA: northern tropical Atlantic mode. SSA: subtropical South Atlantic mode. STA-EQ: equatorial component of southern tropical Atlantic mode. STA-BG: Benguela component of southern tropical Atlantic mode. NTA II: the second mode of NTA caused by model bias.

Table 3. Summary of best performance models in each aspect of variability evaluation.

Criteria	Best performance models
Seasonal Cycle	NCAR-CCSM4, CSIRO-MK360, GISS-E2H, GISS-E2R, MOHC-HadCM3, MPI-ESM-LR, MPI-ESM-P
rEOF Analysis	NCAR-CCSM4, GISS-E2H
Multidecadal Variability (roughly estimated)	CanESM2, CSIRO-MK360, GFDL-CM3, GFDL-ESM2G, GISS-E2H, GISS-E2R, HadGEM2CC, INMCM4, IPSL-CM5A-LR, IPSL-CM5A-MR, IPSL-CM5B-LR, MPI-ESM-LR, MPI-ESM-P, NCC-NorESM1M
Remote connection with ENSO and NAO	NCAR-CCSM4, GISS-E2H, GISS-E2R, NCC-NorESM1M

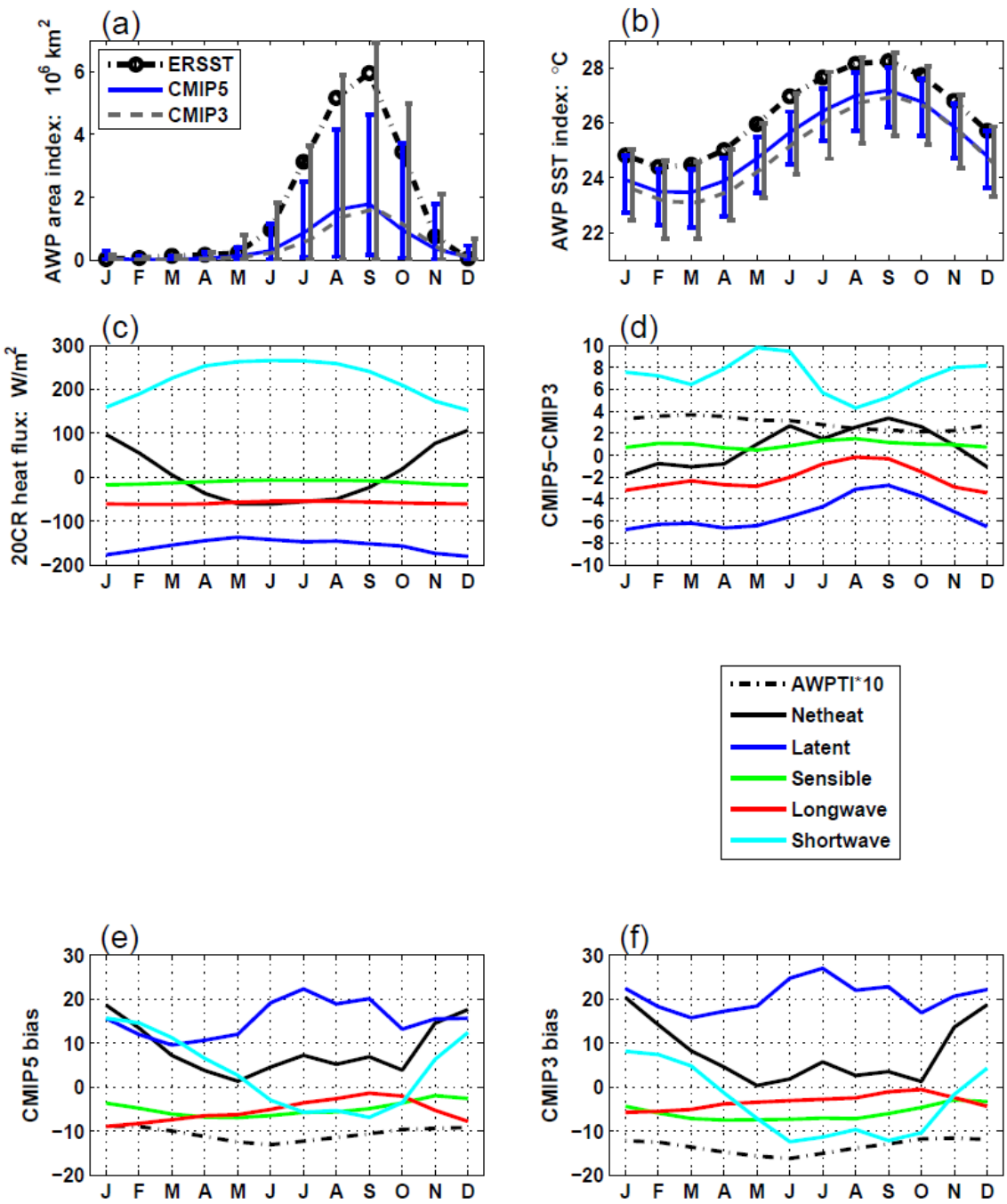

Figure 1 Climatology of (a) AWPAI, (b) AWPTI, AWP box averaged (c) net surface heat flux of 20CR, (d) net surface heat flux of CMIP5 minus CMIP3, (e) net surface heat flux of CMIP5 minus 20CR, (f) net surface heat flux of CMIP3 minus 20CR. Positive value of heat fluxes mean ocean gains heat. AWP box is defined within 5^0N-30^0N and land-40^0W. Black line with circle is for ERSST in (a). Blue line is ensemble of CMIP5 CGCMs. Grey dash is ensemble of CMIP3 models. Model spreads are represented by vertical bars. Black dashed line in (d), (e) and (f) stands for AWPTI*10 in ^{o}C.

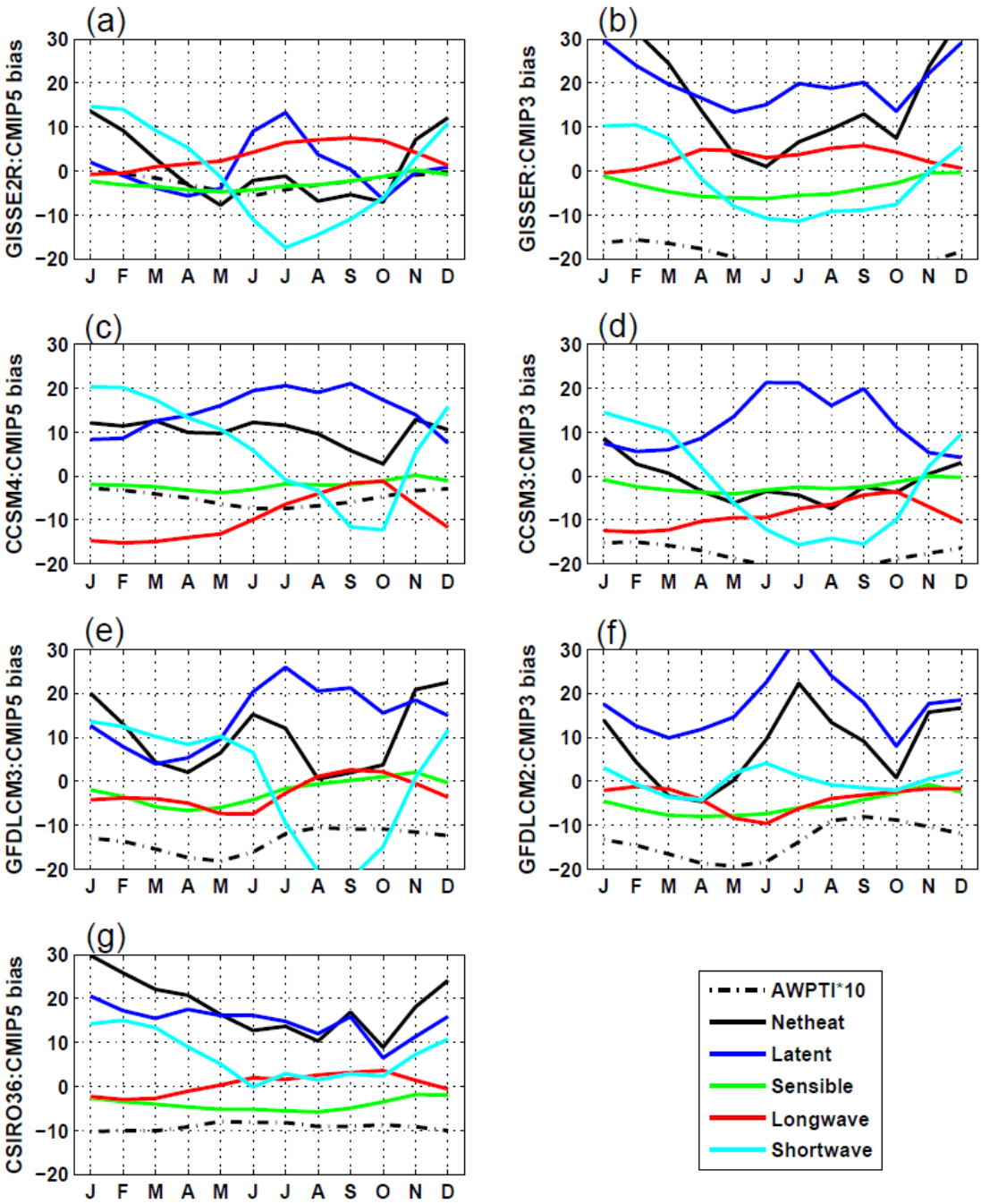

Figure 2 AWP box averaged net surface heat flux bias and AWPTI bias for selected models: (a) GISSE2R_CMIP5, (b) GISSER_CMIP3, (c) CCSM4_CMIP5, (d) CCSM3_CMIP3, (e) GFDLCM3_CMIP5, (f) GFDLCM2_CMIP3, and (g) CSIRO36_CMIP5. Heat flux bias is in Unit W/m^2. AWPTI is in Unit ^{o}C.

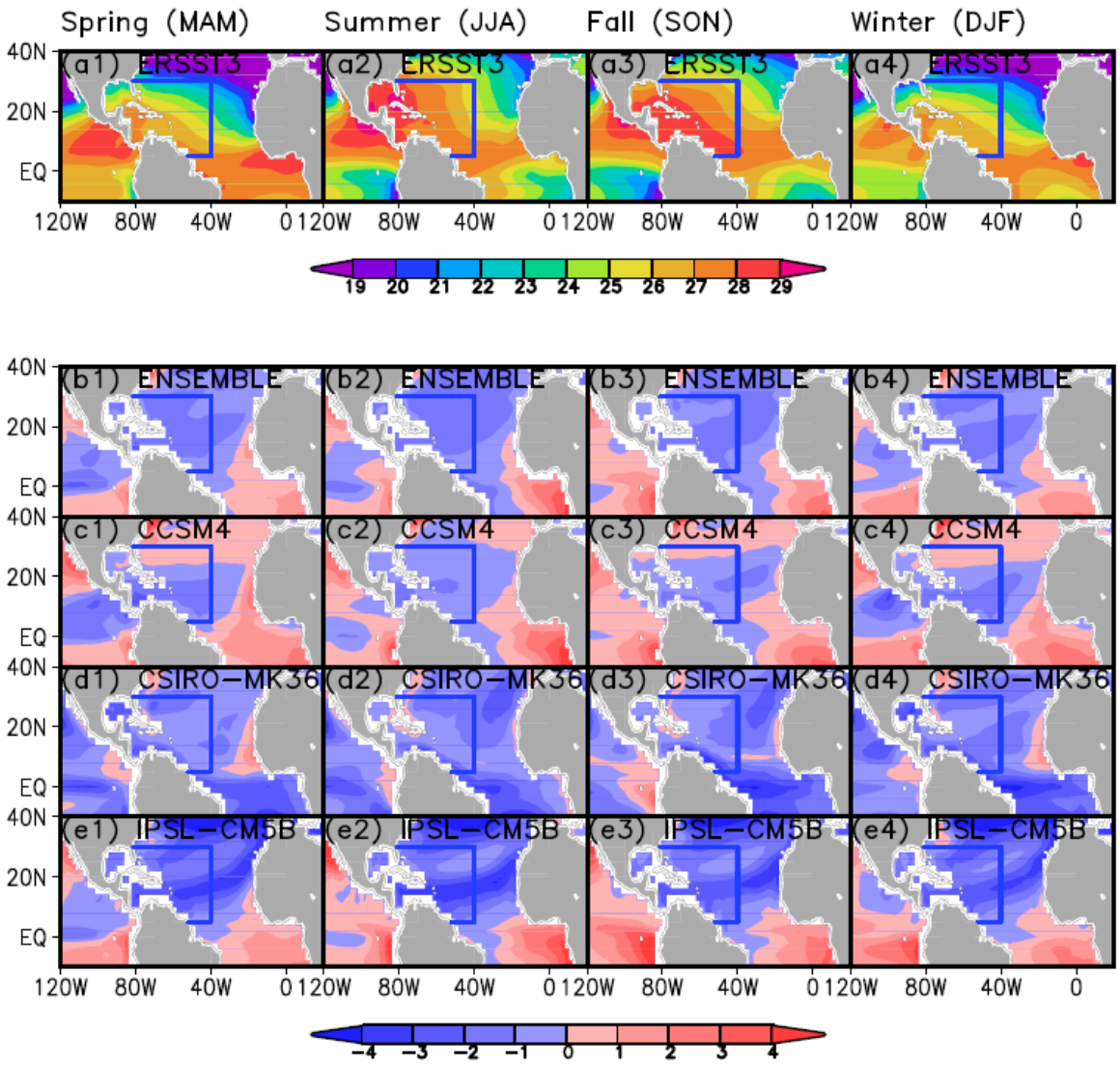

Figure 3 Observational SST and model SST bias in four seasons. Shown are (a1-a4) ERSST SST averaged in four seasons, (b1-b4) the seasonal SST bias of the 19 model ensemble, and (c1-c4, d1-d4, e1-e4) the seasonal SST bias for selected models. Unit is °C. AWPTI is defined in the domain from coast to 40˚W and from 5˚N to 30˚N.

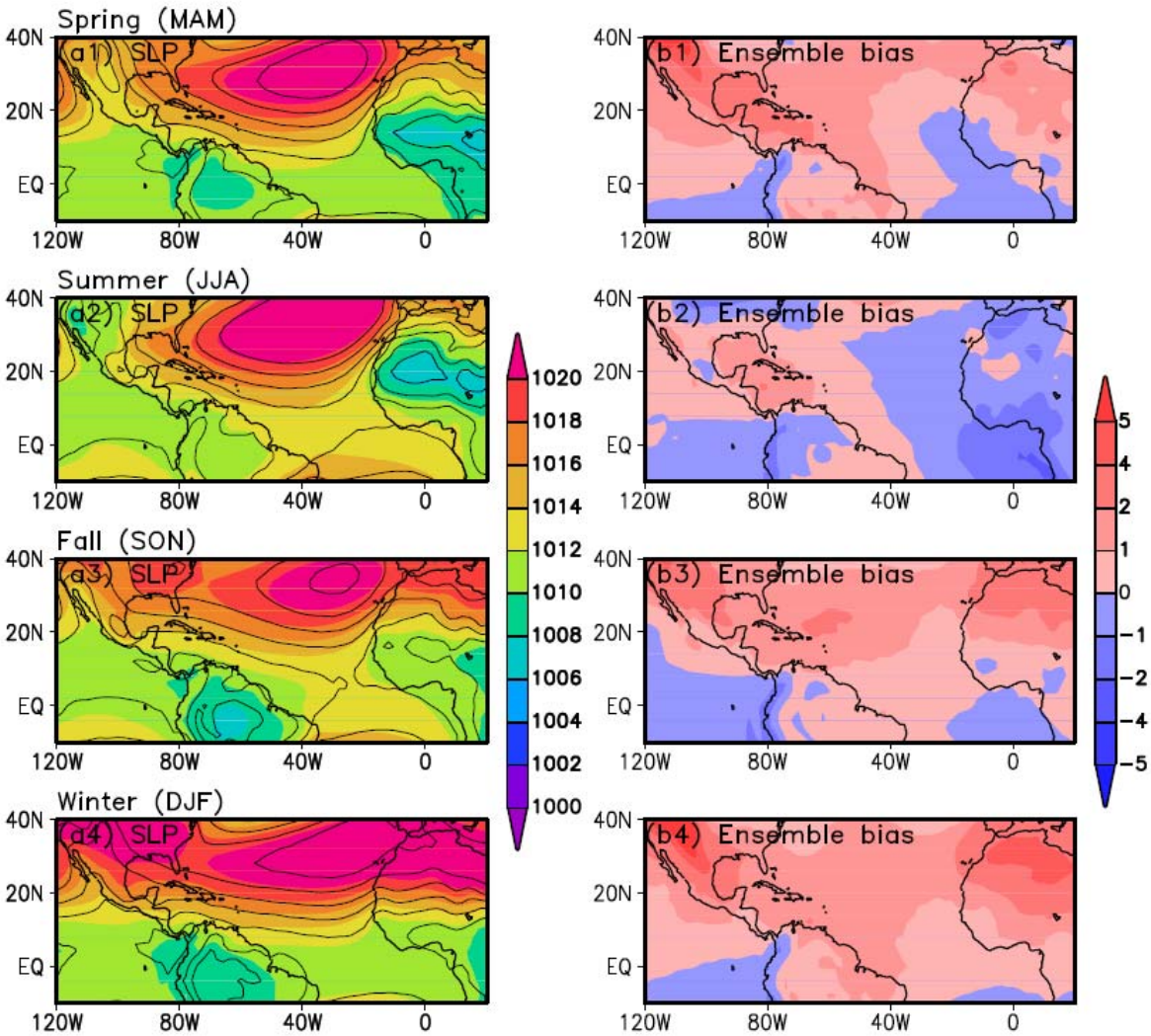

Figure 4. Climatology of SLP and model ensemble bias. (a1-4) are climatology of SLP. Shading stands for model ensemble. Contour lines stand for 20CR. (b1-4) are model ensemble bias for four seasons compared with 20CR. Unit is hPa.

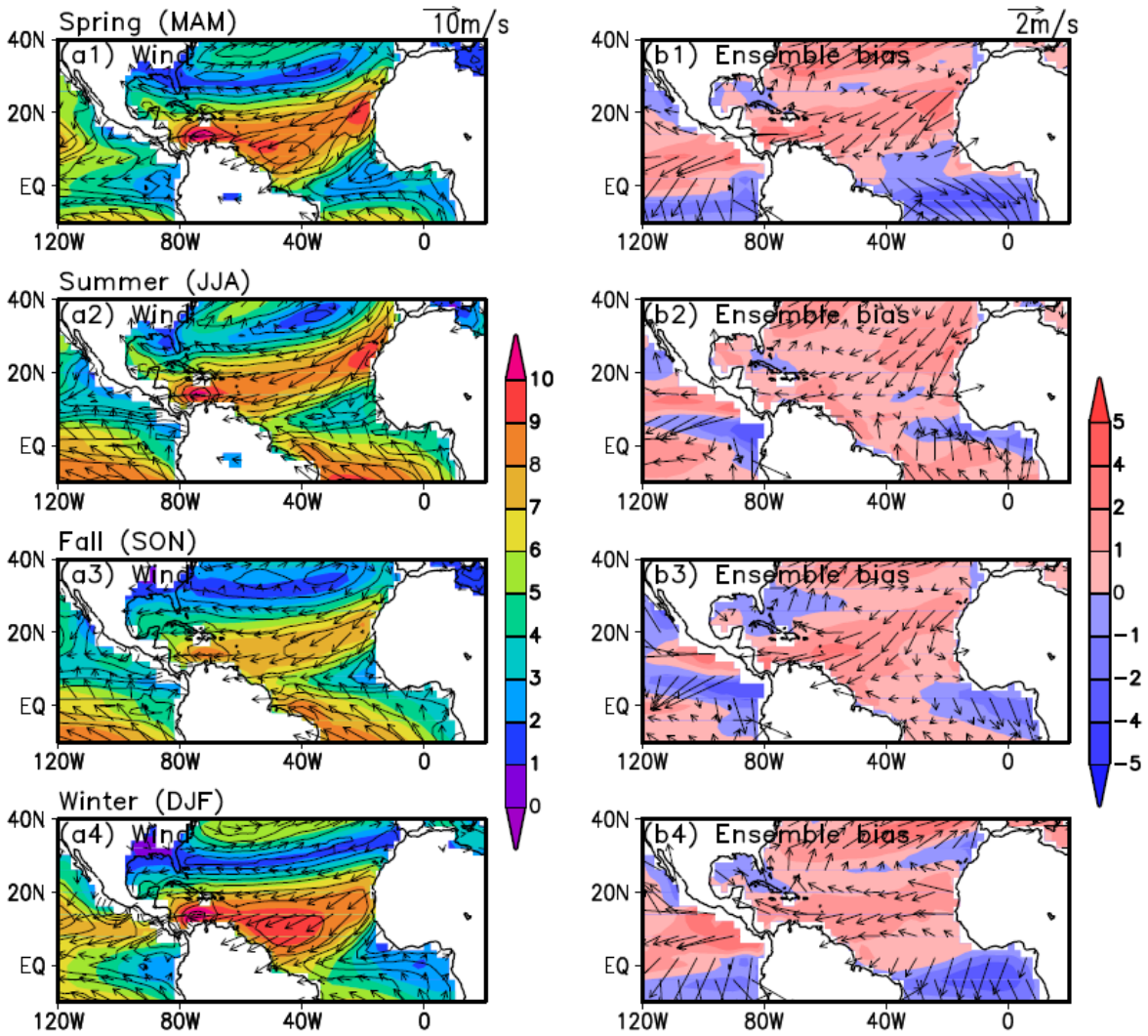

Figure 5 Climatology of surface winds and model ensemble bias. (a1-4) are climatology of surface winds. Shading stands for wind speed of model ensemble. Vectors stand for wind vectors of model ensemble. Contour lines stand for wind speed of IFREMER data. (b1-4) are model ensemble bias for four seasons compared with IFREMER data. Shading stands for wind speed bias and vectors stand for wind vector bias. Unit is m/s.

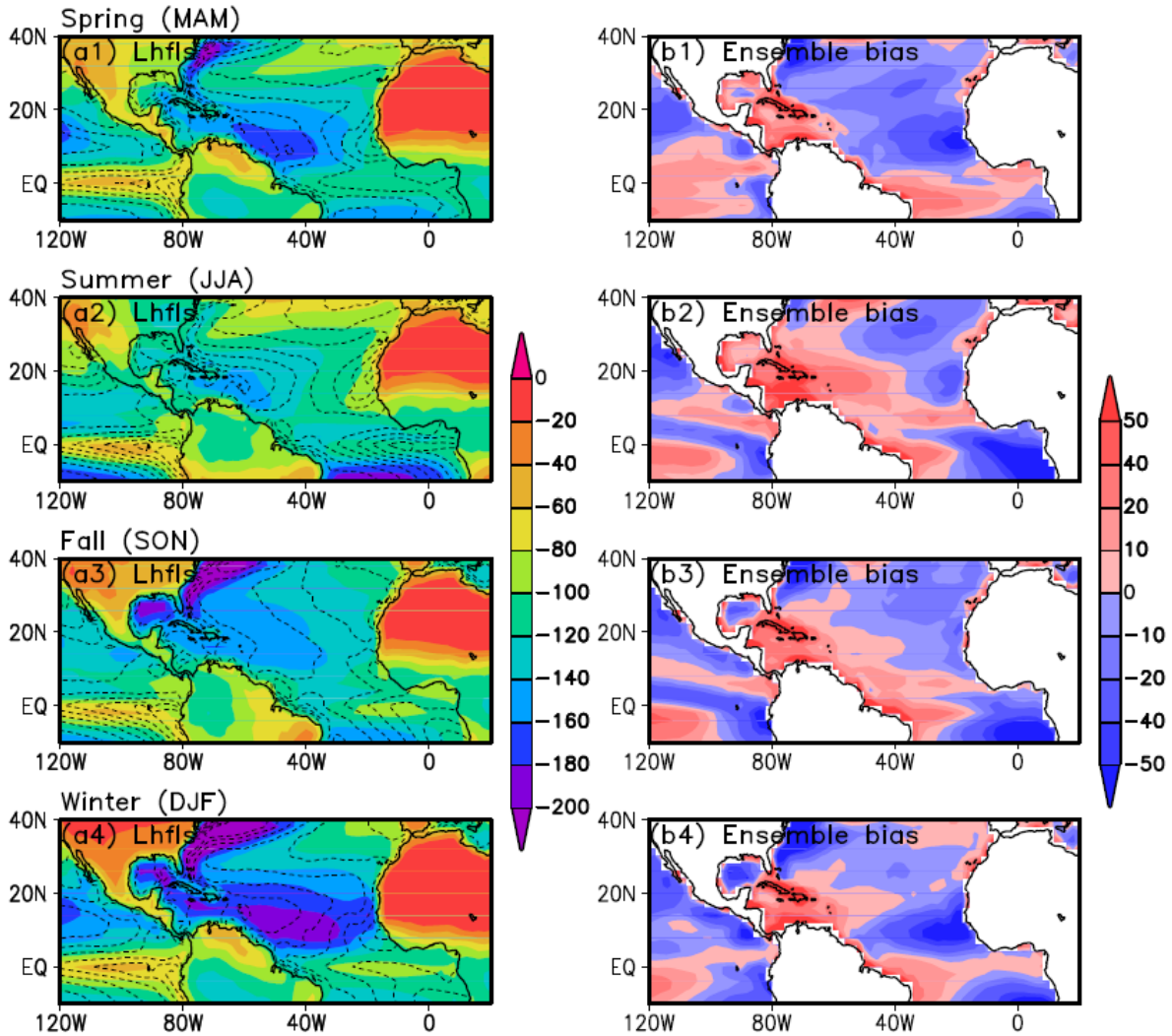

Figure 6 Climatology of latent heat flux and model ensemble bias. (a1-4) are climatology of latent heat flux. Shading stands for model ensemble. Contour lines stand for IFREMER data. (b1-4) are model ensemble bias for four seasons compared with IFREMER data. Unit is W/m^2.

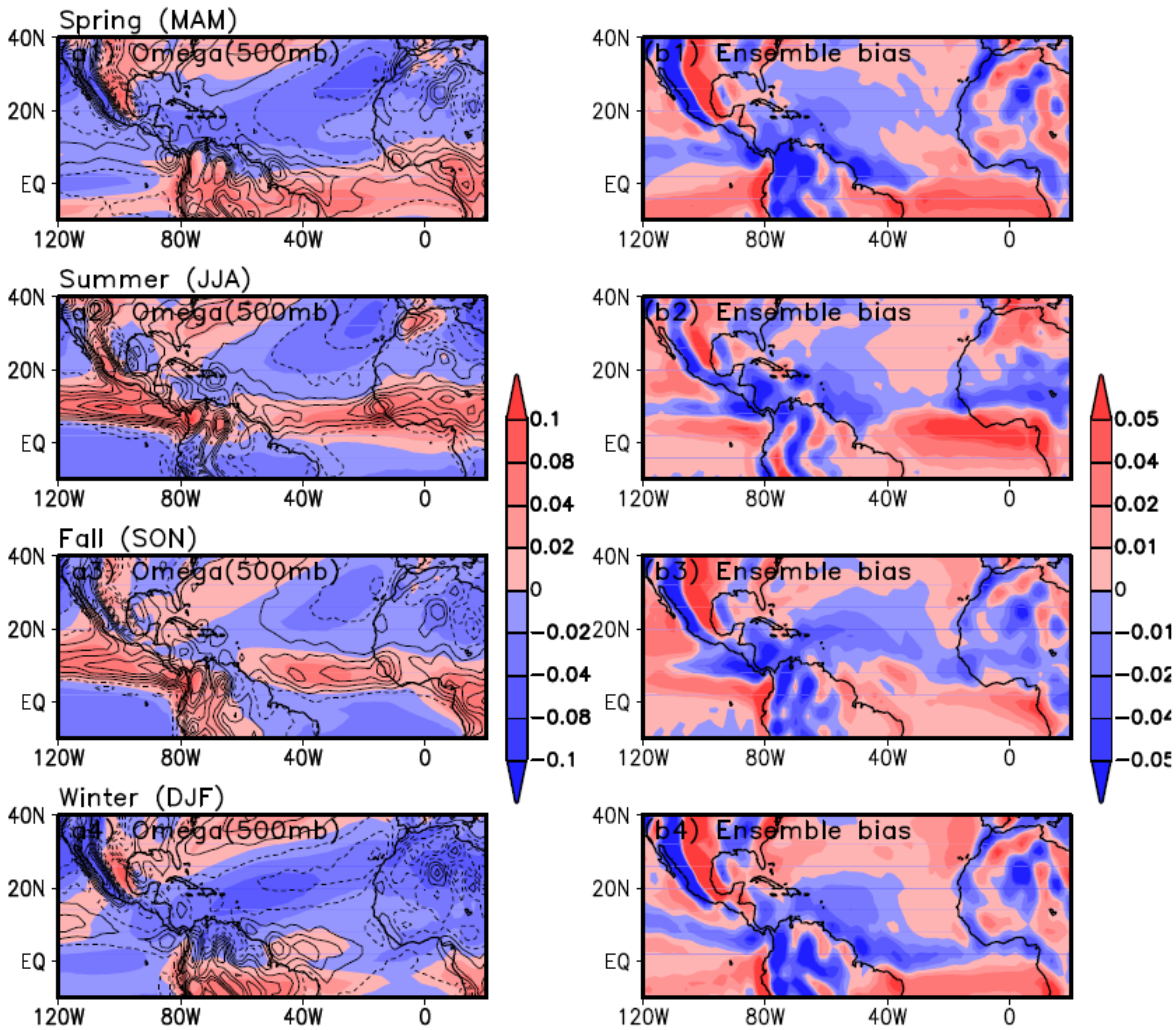

Figure 7 Climatology of pressure vertical velocity and model ensemble bias. (a1-4) are climatology of pressure vertical velocity. Shading stands for model ensemble. Contour lines stand for 20CR. (b1-4) are model ensemble bias for four seasons compared with 20CR.The sign of pressure vertical velocity is reversed and subsidence corresponds to negative pressure velocity. Unit is Pa/s.

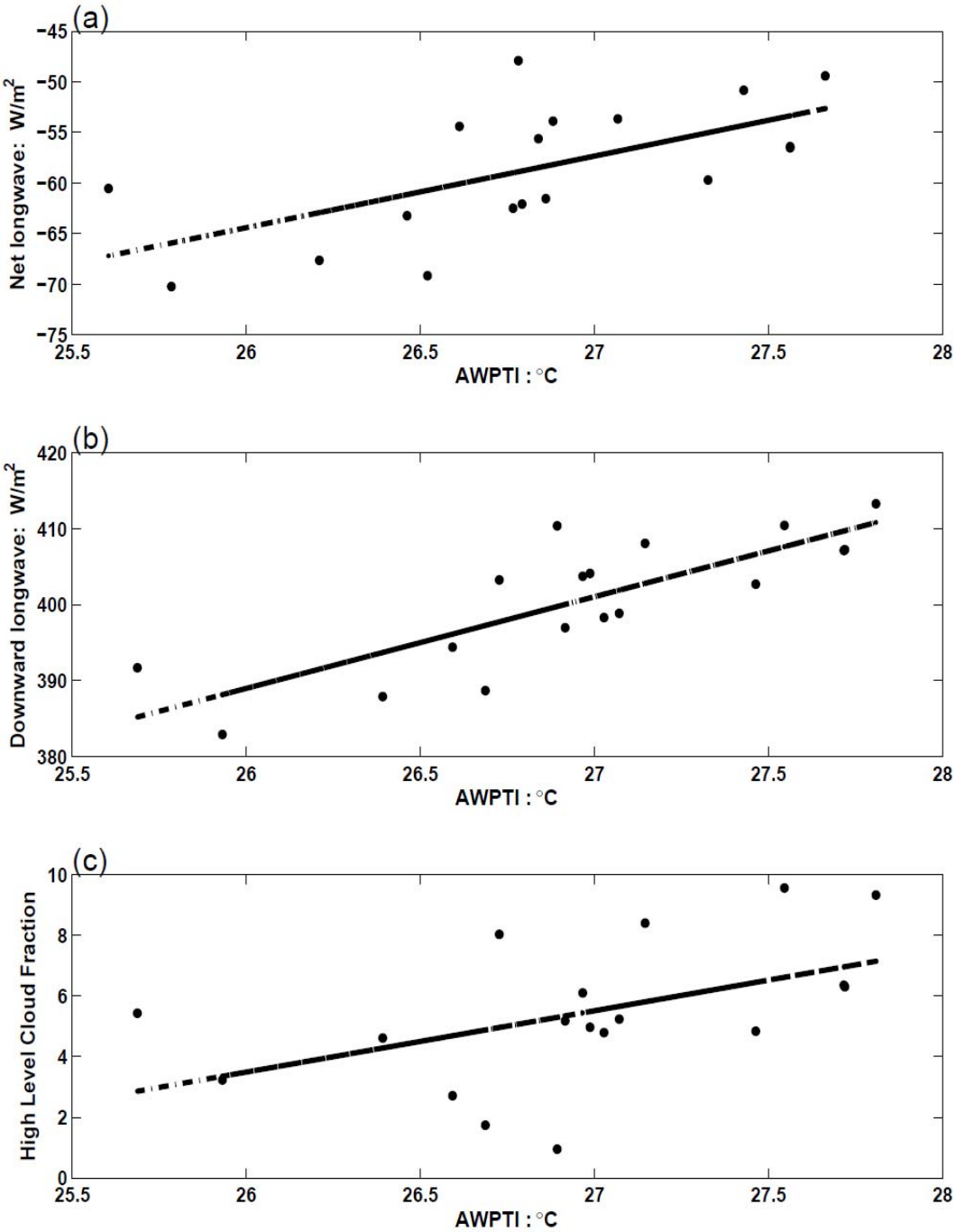

Figure 8 Multi-model scatter plot in JASO of (a) net longwave radiation vs. AWPTI, (b) downward longwave radiation vs. AWPTI, and (c) high level cloud fraction vs. AWPTI. Each point stands for one model. The black line shows the least squares linear fit to all points.

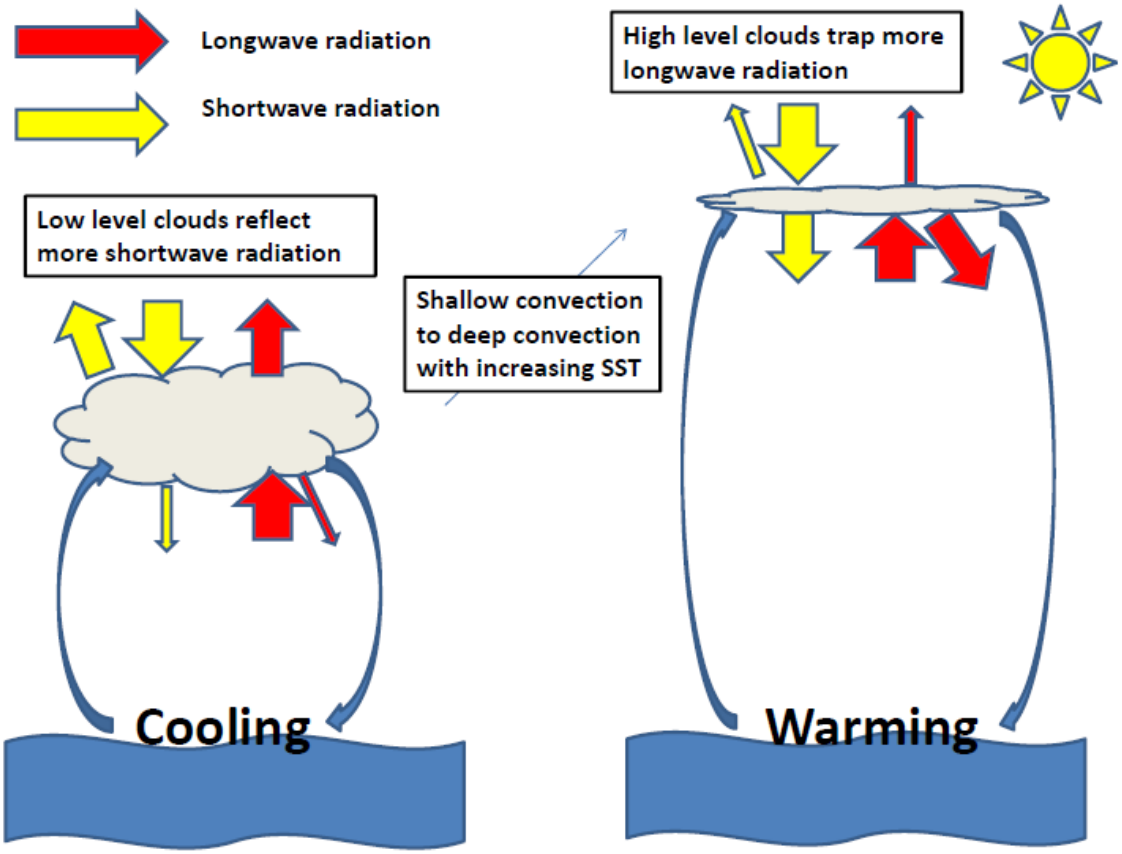

Figure 9 Diagram of different radiative properties of low and high level clouds and their associated feedback with SST in the AWP region.

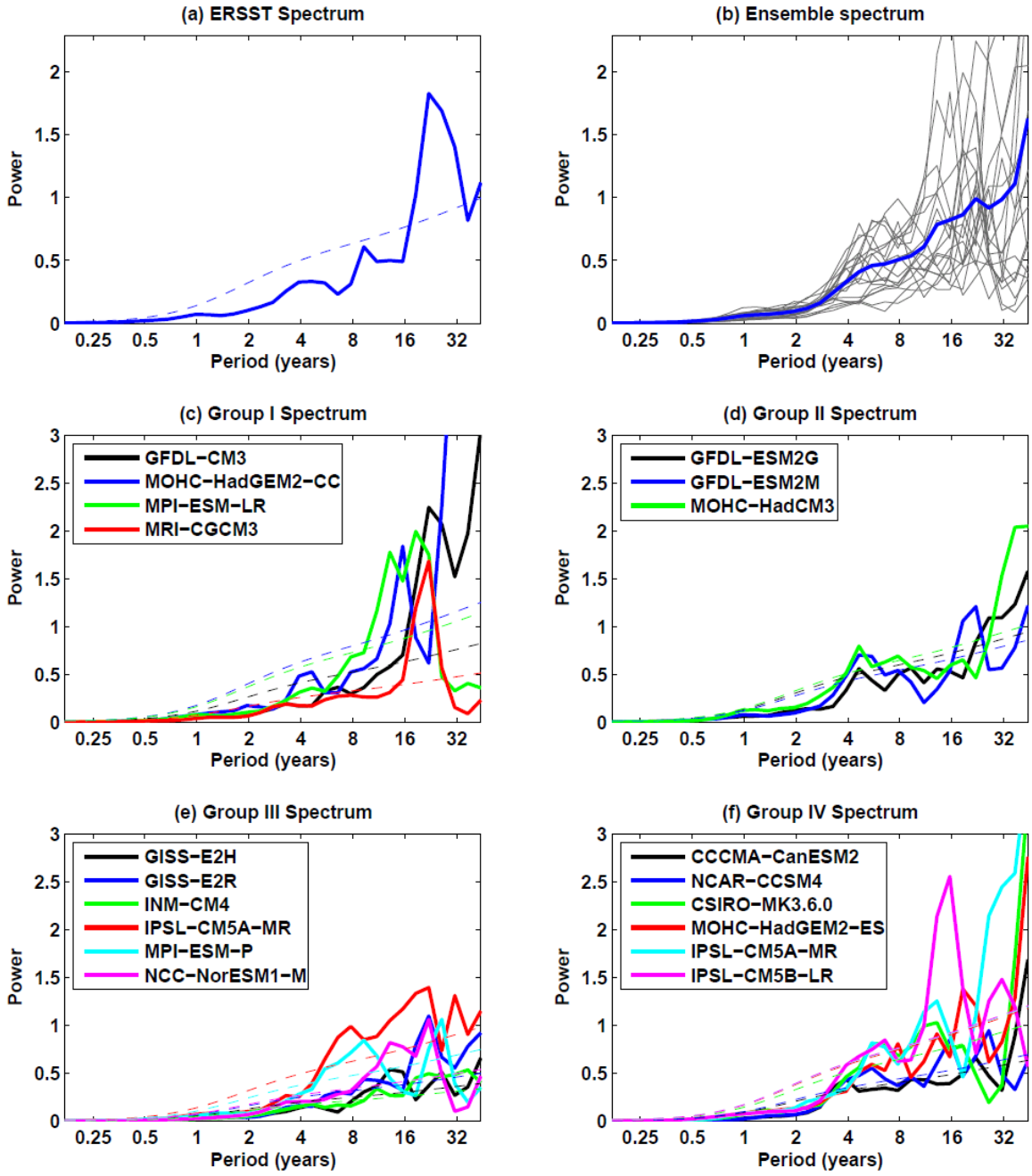

Figure 10 Spectrum analysis of AWPTI. (a) spectrum of ERSST. Y axis is power. X axis is the wavelet period in years. The dashed line indicates 95% significance level. (b) (c), (d) and (e) are the same as (a) for the ensemble of 19 models with each model shown in grey line, Group I, Group II, Group III and VI models respectively.

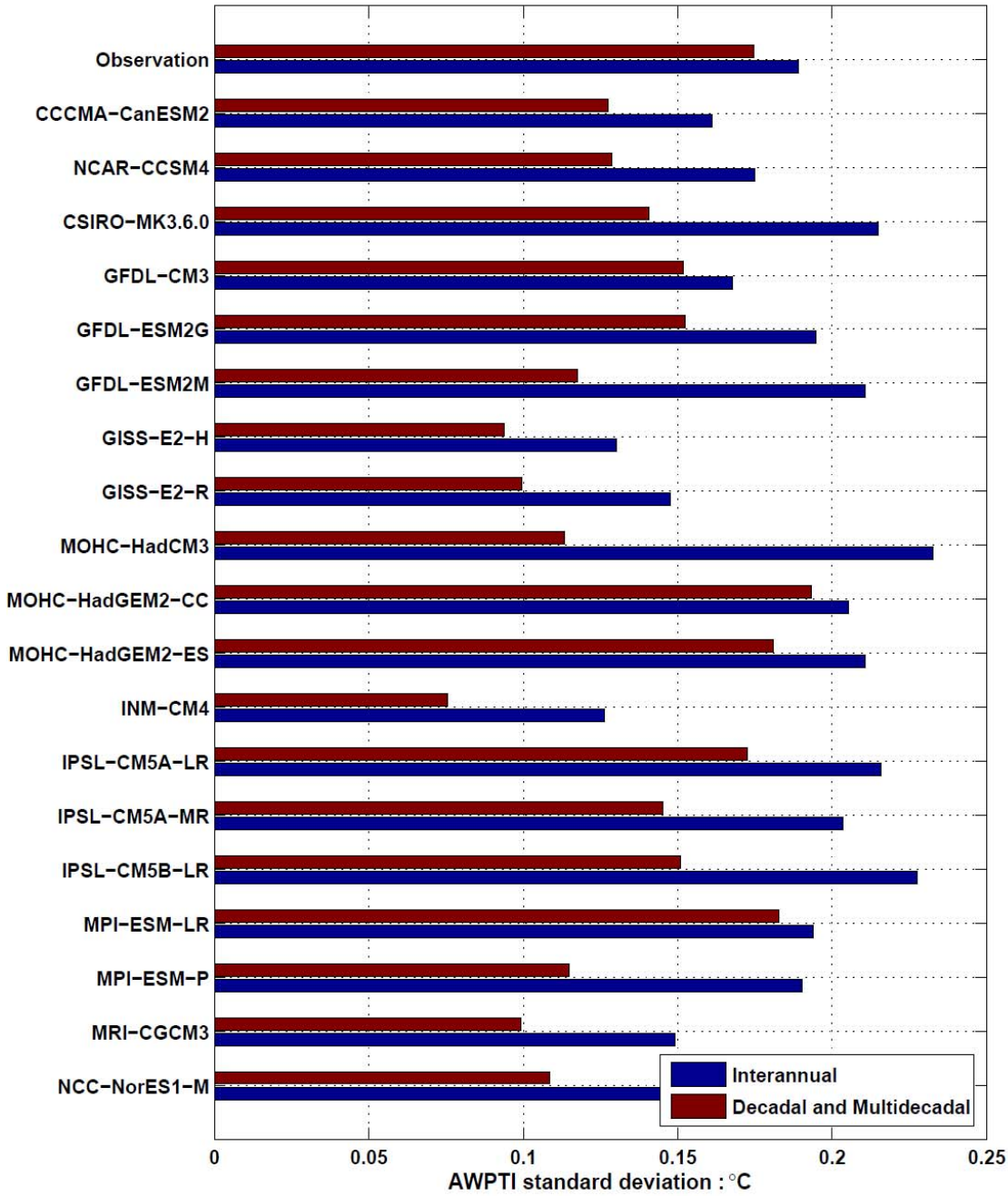

Figure 11 AWPTI standard deviation of observations and CGCMs. Blue bar shows interannual band. Red bar shows decadal and longer time scale band.

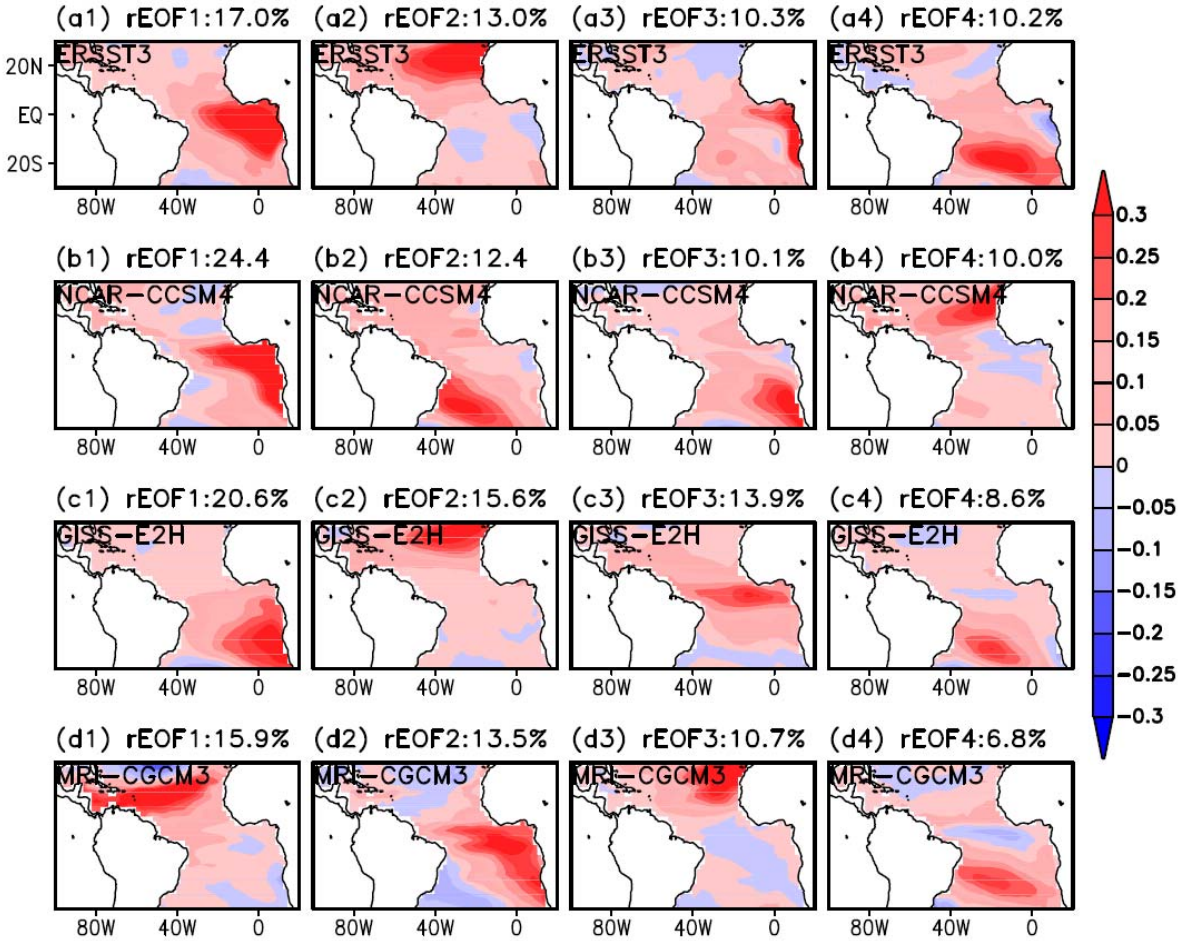

Figure 12 rEOF analysis of tropical Atlantic SST in ASO months. Shown are (a1) first mode, (a2) second mode, (a3) third mode and (a4) fourth mode of ERSST. Same as (a1-4), (b1-4) are for NCAR-CCSM4, (c1-4) are for GISS-E2H, (d1-4) are for MRI-CGCM3.

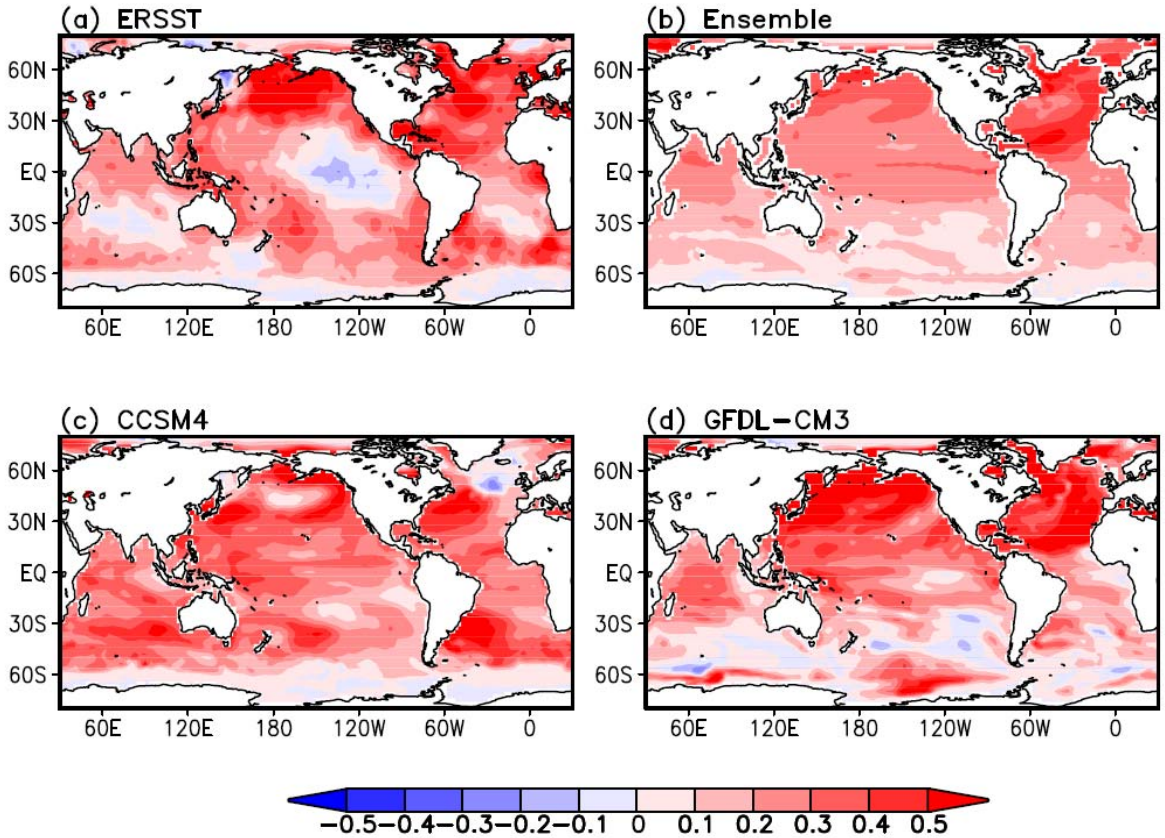

Figure 13 Pattern of global SST difference between large AWP years and small AWP years on the decadal timescale and above. Shown are (a) ERSST, (b) ensemble of 19 models, (c) NCAR-CCSM4 and (d) GFDL-CM3. Unit is ^{o}C. The threshold value of AWPTI to define large(small) AWP years is 0.1^{o}C (-0.1^{o}C).

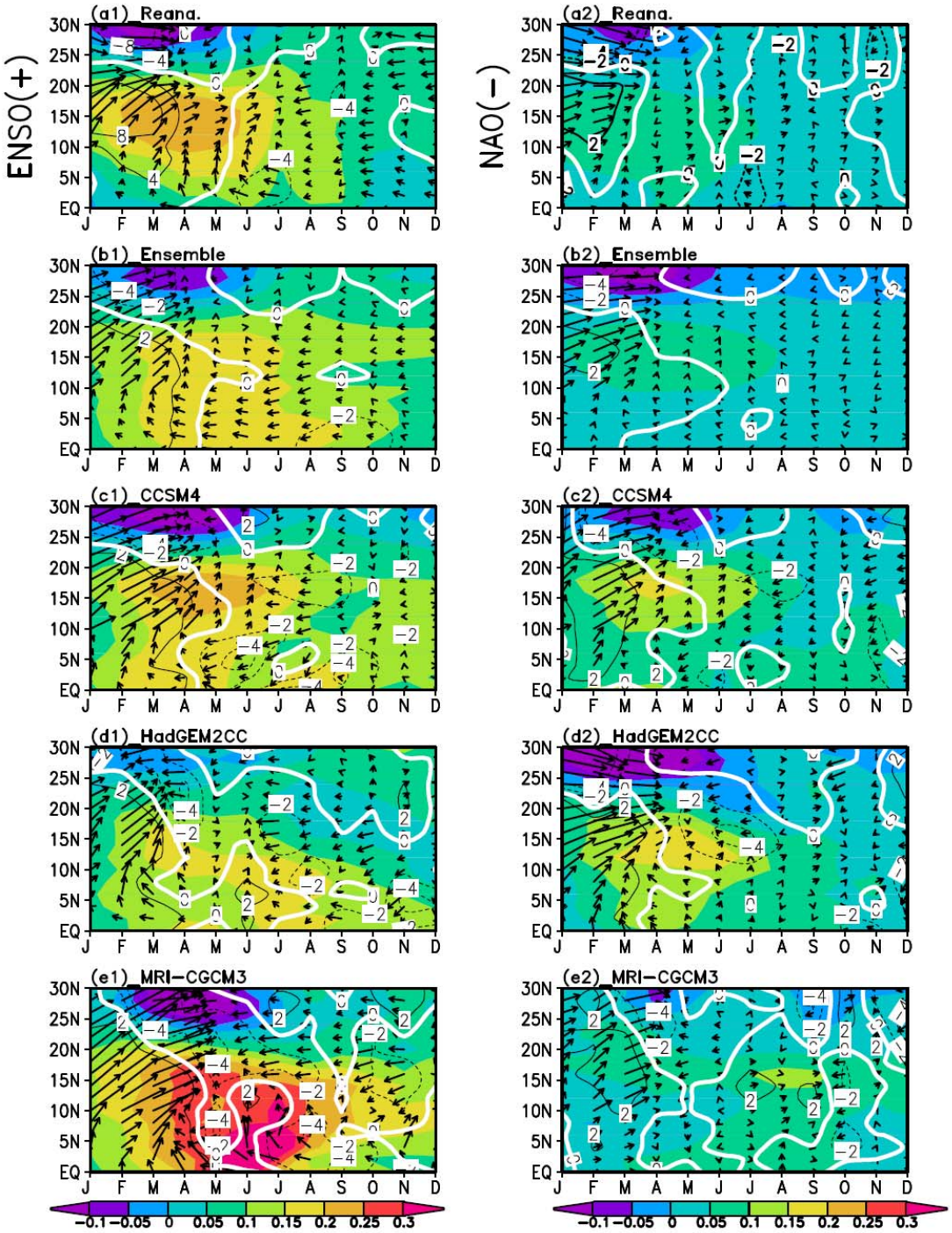

Figure 14 Regression map of surface wind stress (vector, N/m^2), net surface heat flux (positive into the ocean with solid contour line, W/m^2), and SST (shading contour, ^{o}C) averaged in longitude onto Niño-3 Index (DJF) and onto negative NAO index (DJFM). Shown are (a1) regression map onto Niño-3 Index for observations, (a2) regression map onto negative NAO Index for observations, (b1) regression map onto Niño-3 Index for ensemble of 19 models, (b2) regression map onto negative NAO Index for ensemble, (c), (d) and (e) are the same as (b) for

selected models.

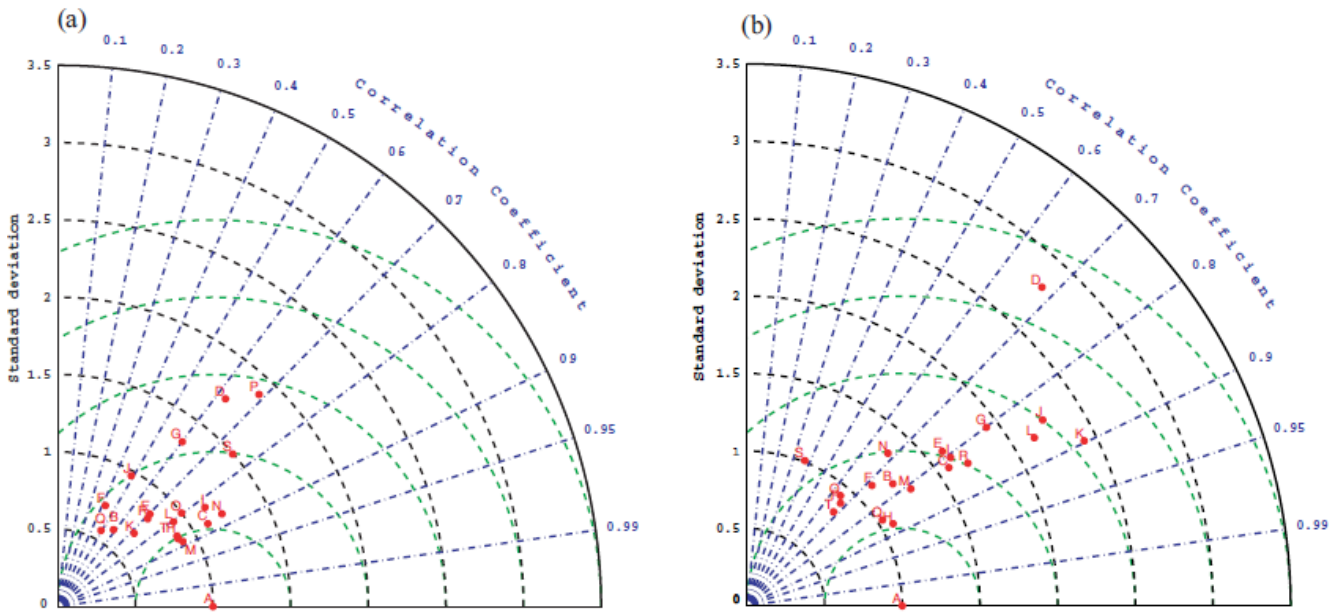

Figure 15 (a) A Taylor diagram of statistics describing the remote influenced patterns of ENSO on AWP in CGCMs as shown in Figure 14.a.1. On this diagram, the radial co-ordinate gives the magnitude of total standard deviation of lag regression coefficients in the domain of Figure 14.a.1 for each model normalized by the standard deviation of observation, and the angular co-ordinate gives the correlation of the regression coefficients of each model with the regression coefficients of observation. The distance between the reference point "A" of observation and any model's point (B to T defined in Table 1) is proportional to the root mean square error shown by the green dashed lines. (b) Same as (a), but the statistics of Taylor diagram describing the remote influenced patterns of NAO on AWP in CGCMs as shown in Figure 14.a.2.